Icarus 375 (2022) 114810

Contents lists available at ScienceDirect

Icarus

journal homepage: www.elsevier.com/locate/icarus

Research Paper

3D Monte-Carlo simulation of Ganymede's water exosphere

Audrey Vorburger [a,b,*], Shahab Fatemi [a], André Galli [b], Lucas Liuzzo [c], Andrew R. Poppe [c], Peter Wurz [b]

[a] Department of Physics, University of Umeå, Umeå, Sweden
[b] Physics Institute, University of Bern, Bern, Switzerland
[c] Space Sciences Laboratory, University of California, Berkeley, Berkeley, CA, USA

ARTICLE INFO

Keywords:
Ganymede
Exosphere
Sputtering
Sublimation
Monte-Carlo model

ABSTRACT

In this paper we present *ab initio* 3D Monte-Carlo simulations of Ganymede's surface sputtered and sublimated H_2O exosphere. As inputs, we include surface water content maps and temperature distribution maps based on Galileo and Very Large Telescope (VLT) observations. For plasma precipitation, we use hybrid model results for thermal H^+ and O^+, energetic H^+, O^{++}, S^{+++}, and electrons, with unprecedented energy resolution. Our results show that up to a solar zenith angle of ~60° and up to ~600 km altitude, sublimated H_2O dominates the atmosphere by up to four orders of magnitudes in number density, while sputtering dominates elsewhere. Sputtering is mainly induced by the impinging O^+, O^{++}, and S^{+++} ions, while protons (H^+) and electrons only add about 1% of the total sputtered H_2O molecules to the atmosphere. Electrons are thus not important for the generation of the atmosphere, but they are important for spectroscopic observability of the atmosphere since they are the main inducer of the Lyman-α and O I emission lines. The extended H_2O atmosphere at altitudes $\gtrsim$1 Ganymede radius is mainly the result of sputtering by thermal O^+ ions, which is the only ion species with substantial fluxes in the low-energy range (10 eV–10 keV), i.e., is the only species that efficiently induces nuclear sputtering. Most released H_2O molecules return to the surface where they immediately adsorb, not forming a thermalized atmosphere. The morphology of Ganymede's magnetosphere, and the resulting dichotomies in the surface fluxes of the precipitating magnetospheric particles (polar fluxes > equatorial fluxes and leading equatorial fluxes > trailing equatorial fluxes), are thus well discernible in the sputtered atmosphere, persisting up to altitudes of a few thousand kilometers. In-situ measurements, as they are planned for the upcoming JUpiter ICy Moons Explorer (JUICE) mission, will mainly probe this sputtered atmosphere, except for encounters with the near-surface atmosphere on Ganymede's day-side, where the sublimated atmosphere will be probed instead. Finally, we compare our model results to the first observational evidence for a sublimated H_2O atmosphere on Ganymede, and find a very good agreement.

1. Introduction

Ganymede is the only known satellite in the solar system that possesses a strong magnetic field of internal origin, with a surface magnetic field of ~720 nT near the equator (Gurnett et al., 1996; Kivelson et al., 1996, 2002). The interaction between this strong field and the co-rotating magnetospheric plasma flow of Jupiter forms a small magnetosphere embedded within Jupiter's much larger magnetosphere (Kivelson et al., 2004).

The surface of Ganymede can be divided into two major terrains: the brighter, ice-rich, younger high-latitude terrain covering approximately 65% of the surface, and the older, mineral-rich, darker low-latitude terrain covering approximately 35% of the surface (Shoemaker et al., 1982; Carlson et al., 1996). Detailed analysis of the optical spectra has confirmed that Ganymede's surface composition is dominated by two constituents: H_2O-ice and an unidentified darkening agent (e.g., Pilcher et al., 1972; Kieffer and Smythe, 1974; Lebofsky, 1977; Pollack et al., 1978; Calvin and Clark, 1991; Calvin et al., 1995; Helfenstein et al., 1997; McCord et al., 2001; Pappalardo and Barr, 2004; Stephan et al., 2017). Less abundant constituents include carbon dioxide, sulfuric acid hydrate, sulfates, and chlorinated salts (hydrocarbons, hydrogen sulfide, 'altered' sulfur materials, tholins or sulfate salts, and other sulfur-oxygen minerals) (McCord et al., 1997; McCord et al., 1998; Domingue et al., 1998; Hibbitts et al., 2003). The surface temperature ranges from ~80 K to 152 K, though extensive analyses of the thermal properties of the ice present on Ganymede's surface suggest that the

* Corresponding author at: Department of Physics, University of Umeå, Umeå, Sweden.
E-mail address: audrey.vorburger@unibe.ch (A. Vorburger).

https://doi.org/10.1016/j.icarus.2021.114810
Received 30 July 2021; Received in revised form 15 October 2021; Accepted 17 November 2021
Available online 13 December 2021

maximum temperature may be lower, with values as low as 112 K proposed by some studies (Spencer, 1987; Orton et al., 1996).

Similar to other outer planetary moons, Ganymede's icy surface is subject to sublimation as well as weathering processes including thermal and energetic plasma impact, electromagnetic radiation, exposure to photons and micro-meteoroid bombardment (see e.g., Galli et al., 2021). Voyager 2, Galileo, and JUNO spacecraft imaging of Ganymede's surface showed that Ganymede's polar cap regions are brighter than the equatorial region, and that the trailing hemisphere is darker than the leading hemisphere near the equator (Smith et al., 1979; Hansen and McCord, 2004; Khurana et al., 2007; Alday et al., 2017; NASA, 2021). Among several proposed theories to explain this dichotomy (e.g.,Khurana et al. (2007)), Ganymede's magnetosphere has shown to play a major role in protecting the equatorial regions from the incidence of plasma while enabling the access of Jovian plasma flux into the polar caps (Cooper et al., 2001; Fatemi et al., 2016; Poppe et al., 2018; Carnielli et al., 2020b; Plainaki et al., 2015, 2020).

In line with this, multiple observations of auroras on Ganymede have shown the auroras to be very heterogeneous. The auroras, the brightness of which is determined by both the atmospheric density and the differential electron flux, are brightest at relatively high latitudes on the trailing hemisphere and are confined to lower latitudes on the leading hemisphere (McGrath et al., 2013). These auroral heterogeneities corroborate the complexity of both the plasma and energetic particle environment near (and interaction with) Ganymede as well as the non-uniformity of Ganymede's atmosphere.

Modeling of Ganymede's atmosphere is thus non-trivial. The sputtered atmosphere strongly depends on the plasma precipitation pattern, which is determined by the interaction between the Jovian plasma and Ganymede's intrinsic magnetic field, and therefore must be determined from modeling efforts. In addition, while the sublimated atmosphere is not affected by the complex plasma environment, the Sun-plasma angle constantly changes as Ganymede orbits Jupiter, adding another level of complexity to the course of interaction.

1.1. Observations

So far only three constituents of Ganymede's atmosphere have been observed: Hydrogen, oxygen, and water.

Hydrogen was observed via Lyman-α emission with the Galileo/Ultraviolet Spectrometer (Barth et al., 1997) and with the Hubble Space Telescope (HST) / Space Telescope Imaging Spectograph (Feldman et al., 2000; Alday et al., 2017). The Lyman-α emissions were observed to be well above the Lyman-α sky background out to altitudes of at least 1 R_G, where R_G=2634.1 km is the radius of Ganymede. Observed variations in the hydrogen brightness (between different instruments but also over time for individual instruments) are attributed to (i) a non-uniform distribution of Ganymede's H corona, (ii) a change in the H corona over time, (iii) different magnetospheric plasma conditions, or (iv) different instruments and analysis techniques (Alday et al., 2017). As possible source mechanisms, the authors proposed photo-dissociation of H_2O vapor that has sublimated from the surface ice, photo-desorption of surface water ice (either as H_2O with subsequent photo-dissociation or directly as H), and sputtering of water ice by Jupiter's magnetospheric plasma (directly as H).

The oxygen observations are more numerous than the hydrogen observations. Oxygen was observed via (i) OI 1304 and OI 1356 Å airglow observations (Hall et al., 1998; McGrath et al., 2013; Molyneux et al., 2018), (ii) 6300 and 6363 Å atomic oxygen emission lines (Brown and Bouchez, 1999), and (iii) 1160–1720 Å spectral images (Feldman et al., 2000). Emissions are brightest at relatively high latitudes (~(40–50)° latitude) on the trailing hemisphere in an auroral oval that extends to as low as ~10° north (~(10–30)° latitude) on the leading hemisphere. On average, the total disk brightness is ~1.4 times brighter on the leading than on the trailing hemisphere, and the sub-Jovian hemisphere is ~1.4–1.8 times brighter than the anti-Jovian hemisphere. The large-scale, nominal auroral ovals seem to be quite stable on a multiyear time-scale, despite the observations showing significant brightness fluctuations on short timescales and long-term temporal variations correlated to Ganymede's changing magnetic latitude (McGrath et al., 2013). Overall, the location of Ganymede's aurora follows the predicted location of the open-closed field line boundary nicely (Eviatar et al., 2001; Khurana et al., 2007; McGrath et al., 2013).

Most recently, Roth et al. (2021) presented the first observational evidence for a sublimated water atmosphere on Ganymede using HST observations. In their study, the authors observed the OI 1356 Å/OI 1304 Å emission line ratios of Ganymede right before and in eclipse (using the Cosmic Origins Spectograph), as well as separately on the leading and the trailing hemisphere (using the Space Telescope Imaging Spectograph). From these emission ratios and from minimal-assumption models, Roth et al. (2021) determine the O_2, O, and H_2O surface and column densities required to reproduce the measured line ratios. For the model part, the authors assumed a scale height of 50 km and an electron temperature and density of 100 eV and 20 cm^{-3}, respectively. The water density is assumed to radially decrease from the sub-solar point with a $\cos^6$ dependence. Their analysis results in maximum sublimated H_2O surface densities of 1.2 $\cdot 10^9$ cm^{-3} on the trailing hemisphere and 2.0 $\cdot 10^8$ cm^{-3} on the leading hemisphere, as well as column densities of several 10^{15} cm^{-2} at the sub-solar region.

1.2. Previous models

Previous models have mainly concentrated on Ganymede's water related atmosphere, taking both sublimation and sputtering, arguably the two most important exospheric source processes on Ganymede, into account. Overall, the models agree on the setup of the atmosphere: In the sub-solar region the atmosphere is dominated by sublimated H_2O molecules, whereas at higher solar zenith angles the atmosphere is dominated by sputtered O_2 close to the surface and by H_2 at higher altitudes (e.g., Marconi (2007)). In addition, the atmosphere was found to be only locally collisional, i.e., near the sub-solar point, being collision-less elsewhere (Marconi, 2007; Shematovich, 2016; Leblanc et al., 2017).

Earliest modeling efforts of Ganymede's atmosphere date back to the 1970's, when Yung and McElroy (1977) published a hydrostatic, spherically symmetric, isothermal diffusive model of Ganymede's O_2 atmosphere. Since then models have become significantly more detailed and extensive, incorporating information now available both from observations as well as from laboratory measurements. More recent models include the model published by Marconi (2007), a multi-species 2D axi-symmetric kinetic model, which accounts for all kinetic regimes (the collisional, the quasi-collisional, and the collision-less). The authors, who investigated the composition, structure, dynamics and escape of both sublimated and sputtered H_2O, OH, O_2, H_2, O, and H, find that except for a small region near the sub-solar point, the atmosphere is quasi-collisional or collision-less. In general, within ~70° of the sub-solar point, the atmosphere is dominated by sublimated H_2O, and elsewhere by O_2 at low altitudes and by H_2 at high altitudes. Using a collision-less 3D parallel test-particle model, Turc et al. (2014) also analyzed Ganymede's sublimated and sputtered water-ice atmosphere, and found similar results regarding the kinetic regimes and the structural makeup (i.e., H_2O dominating close to the sub-solar region, and O_2 and H_2 dominating elsewhere) as (Marconi, 2007). In addition, the authors studied Ganymede's atmospheric response to time-varying parameters, i.e., Ganymede passing into the shadow of Jupiter and intrinsic variations in the Jovian plasma. Plainaki et al. (2015) investigated both Ganymede's sublimated and sputtered atmosphere in detail, incorporating for the latter a model of the spatially varying energetic H^+, O^+, and S^+ ion precipitation onto Ganymede's surface, computed for a configuration where Ganymede is located close to the center of Jupiter's plasma sheet. Whereas their results overall agree

well with previously published models, their detailed sputter analysis shows that the H_2O morphology closely reflects the precipitation morphology, with the H_2O maximum being located at higher latitudes in the trailing hemisphere than in the leading hemisphere. In a later publication, Plainaki et al. (2020) studied high-energy ion precipitation maps for further relative configurations between the moon's magnetic field and Jupiter's plasma sheet, i.e., when Ganymede is above and below the Jovian plasma sheet. These simulations showed that the sputtered H_2O flux can easily be an order of magnitude lower when Ganymede is not close to the center of the plasma sheet. Shematovich (2016) modeled Ganymede's near-surface layer with a kinetic Monte Carlo model that takes collisions into account in the near-surface Knudsen layer. As the previous modelers, Shematovich (2016) investigates both sublimation and sputter sources, but also includes atmospheric sputtering and thermalization of suprathermal atoms. While based on their result the overall structure of the atmosphere agrees with previous model results, inclusion of thermalization of suprathermal atoms results in a substantial increase in the scale height of the dominant component of H_2O and O_2 in the transitional region located at 10–100 km altitude. Leblanc et al. (2017) applied a 3D parallelized collisional model (in fact a modified version of the model presented by Turc et al. (2014)) to determine the spatial distribution of the H_2O and O_2 components in Ganymede's atmosphere (though other species were simulated as well), with a focus on their temporal variability (seasonal variation) along Ganymede's revolution around Jupiter. In contrast to the previous version of the model, where sputtering was assumed to take place at latitudes above 45°, their model accounts for a more complex S^{n+} and O^{n+} ion precipitation, with ions reaching lower latitudes in the trailing hemisphere than in the leading hemisphere. Their analysis shows that due to the seasonal variation there is (i) a general atmospheric shift towards dusk, (ii) an O_2'short-term memory', i.e., the shape of the O_2 atmosphere depends on the production earlier in Ganymede's orbit due to the lifetime of O_2 being on the order of Ganymede's orbital period, and (iii) a clear O_2 local dusk over local dawn asymmetry, with a maximum ratio of 3.4 at a Ganymede phase angle of 150°.

In addition, very recently, Carnielli et al. (2019) published a 3D multi-species model for Ganymede's ionosphere. As an input they used the modeled neutral exosphere simulated by Leblanc et al. (2017), which they improved in their Carnielli et al. (2020b) paper by adding collisions between major ions and neutral species in the atmosphere, an interaction that gives rise to an energetic atmospheric O_2 component. According to their simulations, O_2^+ is the most abundant ion species, followed by O^+, H_2^+, and H_2O^+. The majority of the O^+ and O_2^+ ions were found to impact the moon's surface, and can therefore act as an additional sputtering source. The contribution of this additional sputtering source was investigated by Carnielli et al. (2020a) in a follow-up study, who found that the ionospheric ions impact mainly on the leading hemisphere, and provide a global contribution of at least 10% to the sputtering rate, but can, under certain assumptions, even dominate the total sputtering source.

The general picture emerging from these modeling efforts is consistent. In the sub-solar, low altitude regions sublimation dominates, whereas sputtering dominates elsewhere. Reported maximum H_2O surface densities are approximately equal to $(3–10)\cdot10^8$ cm^{-3} for sublimation and $(4–20)\cdot10^3$ cm^{-3} for sputtering (Marconi, 2007; Turc et al., 2014; Plainaki et al., 2015; Shematovich, 2016), while reported maximum H_2O column densities are on the order of $(3–10)\cdot10^{15}$ cm^{-2} for sublimation (Marconi, 2007; Leblanc et al., 2017) and $2\cdot10^{11}$ cm^{-2} for sputtering (Marconi, 2007). Besides 'nominal sublimation', Leblanc et al. (2017) also proposed a 'low sublimation case', where the sublimation rate is significantly reduced. This case primarily represents an H_2O exosphere dominated by sputtering, but could, according to Leblanc et al. (2017), also be 'within the realm of plausibility' for sublimation at Ganymede. In this scenario, the maximum sublimated H_2O column density amounts to $1\cdot10^{14}$ cm^{-2}, i.e., is by a factor (30–100) lower than the above mentioned $(3–10)\cdot10^{15}$ cm^{-2}. In addition, for sputtering, Leblanc et al. (2017) uses a much higher H_2O sputter flux than Marconi (2007), Turc et al. (2014), Plainaki et al. (2015), Shematovich (2016) do: Their average H_2O sputter flux is equal to $8\cdot10^{27}$ H_2O/s while the other authors use sputter fluxes on the order of $(7–15)\cdot10^{25}$ H_2O/s. Accordingly, the maximum sputtered H_2O surface and column densities modeled by Leblanc et al. (2017) are by one to two orders of magnitudes higher than the commonly derived values presented above. Finally, neutral particles escape primarily from the sputtered atmosphere, and H_2O escape rates were computed to be on the order of $(1–10)\cdot10^{24}$ s^{-1}.

Our model adds a few new key aspects that these models have not yet taken into account. First of all, none of the previous models have incorporated sputtering by electrons on Ganymede, which has been shown to be a dominant process on Europa (Vorburger and Wurz, 2018; Davis et al., 2021). Secondly, we directly compare sputtering of H_2O by H^+, O^+, O^{++}, S^{+++}, and electrons to determine which are the key atmospheric driver(s). Thirdly, we have placed significant emphasis on model accuracy regarding the release processes, e.g., we include surface water concentration maps recently published by Ligier et al. (2019), very recent sputter yield measurements (Davis et al., 2021), and a high level of accuracy in the plasma precipitation fluxes with regard to spatial, mass and energy resolutions. Importantly, our approach considers the effect of the local electromagnetic field perturbations generated by Ganymede's interaction with Jupiter's magnetospheric plasma on the precipitating magnetospheric particles, which has been shown to play an important role in their dynamics (Fatemi et al., 2016; Poppe et al., 2018; Liuzzo et al., 2020). Finally, we compare our model results to first observations of sublimated H_2O on Ganymede, which were very recently published (Roth et al., 2021).

2. Model

In this paper we study two release processes: Sputtering (i.e., the collisional or electronic ejection of surface atoms or molecules) and sublimation (the solid- to gas-phase transition of surface atoms or molecules). In the following subsections we first present the Monte-Carlo model that was used to simulate Ganymede's atmosphere, with a focus on the physics of the source and sink mechanisms implemented. We then present the relevant model inputs, starting with the thermal plasma and energetic particle precipitation fluxes incorporated. In the third subsection we present the relevant Ganymede surface properties, i.e., the surface water concentration and the surface temperature, as well as the relevant sputter yields.

2.1. Atmosphere Monte-Carlo model

Our Monte-Carlo model is a collision-free 3D test particle model that was already used to simulate Callisto's atmosphere (Vorburger et al., 2015, 2019) and Europa's atmosphere (Vorburger and Wurz, 2018). In the model, each particle describes an elliptical or hyperbolic orbit under the influence of Ganymede's gravitational field. The non-collisional character of the atmosphere has previously shown to be valid for most part of the atmosphere, with the possible exception of the sub-solar region, where sublimation dominates (see e.g., Marconi (2007)).

2.1.1. Setup

Our spherical simulation domain reaches from Ganymede's surface to Ganymede's Hill radius, which lies close to 32,000 km (~12 R_G) above Ganymede's surface. The simulation domain is subdivided by a grid that is composed of 348 cells along r, 90 cells along θ and 180 cells along ϕ, where r is the distance from Ganymede's center, θ is the latitude (90°S–90°N), and ϕ is the longitude (0°W–360°W). The resolution in θ and ϕ corresponds to the smallest resolution in the precipitation flux maps (2°), and the number of radial bins results in a voxel at the surface that is cubic (has equal length in all dimensions). The voxels

close to the surface thus encompass volumes of ~92 km^3, whereas the voxels at the Hill radius comprise volumes of ~92 km×1200 km^2, with 92 km being in the radial direction. In our simulations, the sub-solar point coincides with the anti-Jovian sub-point (i.e., Ganymede is at local noon along its orbit and the leading and trailing hemispheres are half-lit), Ganymede is located near the center of the current sheet, and the number of test particles used per run is 2 millions.

2.1.2. Sources

As source processes we consider sublimation and sputtering. For each process considered we need to know the production rate a test particle represents, as well as the 3D velocity distribution function from which its initial velocity can be sampled. The production rate (in s^{-1}) is given by the product of the release flux (given in m^{-2}s^{-1}) and the surface area (given in m^2):

$$R = J_{rel} \cdot A, \tag{1}$$

where J_{rel} is the release flux (i.e., either the sublimation (J_{sub}) or sputter (J_{sp}) flux) and where A is the surface area. For both sublimation and sputtering we implement an angular release distribution function of the form $f(\alpha) = \cos(\alpha)$ (with α being the angle to the surface normal), which was shown by Cassidy and Johnson (2005) to be nearly always applicable for sputtering from icy surfaces (see also Sections 17.3.2 and 17.4.2 in Johnson et al. (2013)).

Sublimation. The sublimation flux for water can be computed from the water vapor pressure and the water surface concentration using the following equation:

$$J_{sub} = \frac{p_0}{k_B T} \cdot \overline{v_{th}} \cdot c, \tag{2}$$

Where p_0 is the water vapor pressure (given by Fray and Schmitt (2009)), k_B is the Boltzmann constant, T is the local surface temperature, $\overline{v_{th}}$ is the mean thermal velocity, and c is the water concentration at the given surface area (see Section 2.3.1).

The sublimation velocity distribution is given by the Maxwell–Boltzmann distribution:

$$f(v)d^3v = \left(\frac{m}{2\pi k_B T}\right)^{3/2} \exp\left(-\frac{mv^2}{2k_B T}\right) d^3v, \tag{3}$$

where m is the particle mass (18 u), k_B the Boltzmann constant, and T the local surface temperature ((80–150) K).

Sputtering. The flux of sputtered water molecules is equal to the flux of precipitating particles (ions or electrons) (see Section 2.2), multiplied with the interaction-specific H_2O sputter yield (see Section 2.3.3) and the water surface concentration (see Section 2.3.1):

$$J_{sp} = J_{pr} \cdot Y \cdot c, \tag{4}$$

where J_{pr} is the precipitation flux, Y is the H_2O sputter yield, and c is the water surface concentration.

The sputtered H_2O velocity distribution depends on the incoming particle's mass and energy. In our model, we implemented two velocity distributions, one for nuclear sputtering and one for electronic sputtering. For nuclear sputtering, the energy distribution function for sputtered H_2O is given by Sigmund (1981):

$$f(E)dE = \frac{2UE}{(U+E)^3}\left[1 - \left(\frac{U+E}{E_i}\right)^{1/2}\right] dE, \tag{5}$$

where U is the binding energy (0.055 eV for H_2O according to Reimann et al. (1984)), and E_i is the energy of the incident particle. For electronic sputtering we assume a quasi-thermal energy distribution (equivalent to the thermal velocity distribution given for sublimated particles above) for the sputtered H_2O:

$$f(E)dE = 2\sqrt{\frac{E}{\pi}}\left(\frac{1}{k_B T}\right)^{3/2} \exp\left(\frac{-E}{k_B T}\right) dE, \tag{6}$$

Table 1
Reaction rates for the considered atmospheric processes.

Reaction	Formula	Rate [s^{-1}]
Photo-dissociation	$H_2O + h\nu \rightarrow OH + H$	4.34e−7
Photo-ionization	$H_2O + h\nu \rightarrow H_2O^+ + e^-$	1.22e−8
Electron-dissociation	$H_2O + e^- \rightarrow OH + H$	7.14e−7
Electron-ionization	$H_2O + e^- \rightarrow H_2O^+ + 2e^-$	8.07e−7

but with an additional E^{-2} tail, which was observed in ice sputtering experiments (see e.g. Johnson and Liu (1996), Johnson et al. (2002), Johnson et al. (2013)).

2.1.3. Sinks

As sinks we consider gravitational escape, surface adsorption, ionization and dissociation. A particle is said to have escaped when it reaches Ganymede's Hill radius, the upper boundary of our simulation. When a particle reaches the lower boundary of our simulation, i.e., re-impacts the surface, it can either stick to the surface or be immediately re-ejected at the local surface temperature (see residency times presented in Shi et al. (2009)). For each surface interaction we make a statistical check where we compare the local surface temperature to the ice-line temperature to decide if the particle sticks or not. During a particle's trajectory, it might be ionized or dissociated by the local photon-, electron-, and ion-population. In this paper, we concentrate on the first two reactants (photons and electrons), because they are independent of the model output. The ion population is harder to quantify, rendering the loss rates due to the ionosphere highly uncertain. In addition interactions with Ganymede-related particles was not included in the hybrid model used to calculate the precipitation fluxes either. Omitting interactions with ionospheric particles here as well is thus consistent. We discuss the implications of omitting this additional loss mechanism in Section 4, though.

The photon- and electron-reaction rates implemented herein are presented in Table 1 and contain photo-rates taken from Huebner et al. (1992) and *http://phidrates.space.swri.edu*, electron-fluxes presented by Kivelson et al. (2004), and cross sections published by Itikawa and Mason (2005) as well as McConkey et al. (2008). They are in agreement with the rates published by earlier modelers (see Section 1.2), though these models themselves exhibit some variance, especially where electrons are concerned.

2.2. Plasma precipitation

Fatemi et al. (2016), using a kinetic hybrid model of plasma, calculated the flux of the Jovian ions precipitating to the surface of Ganymede when Ganymede is inside the Jovian plasma sheet. They found an excellent correlation between the ion precipitation flux and Ganymede's surface brightness patterns. Later, Poppe et al. (2018) using the electromagnetic fields obtained from Fatemi et al. (2016) hybrid simulations combined with a test-particle model analyzed the dynamics of the thermal and energetic ion precipitation to the surface of Ganymede for various Jovian ion species including thermal H^+ and O^+ and energetic H^+, O^{++}, and S^{+++} for a broad energy range of incident ions to the surface (10^1–10^5 eV for the thermal ions and 10^3–10^7 eV for the energetic ions, divided into 17 $10^{0.25}$-sized logarithmic bins each). Similarly, Liuzzo et al. (2020) used the outputs obtained from Fatemi et al. (2016) hybrid simulation to study electron precipitation patterns and surface fluxes onto Ganymede. In their simulation, electrons are initialized at a grid on Ganymede's surface with a spatial resolution of 2° in latitude and 4° in longitude. At each of these 8,100 grid points, electrons are initialized at one of 26 discrete energies between 4.5 keV ≤ E ≤ 100 MeV, at a resolution in velocity space of 2° in zenith and 4° in azimuth (trajectories evolve backward in time). For further detail on the particle tracing approach, the reader is referred to the aforementioned publications. In our study, we use the thermal and

energetic ion precipitation maps from Poppe et al. (2018) and the energetic electron maps from Liuzzo et al. (2020) for a configuration where Ganymede is near the center of the current sheet (i.e., for the Galileo G8 flyby configuration). Thanks to the high energy resolution provided, we can make a clear distinction between nuclear and electronic sputtering in our model. The total ion precipitation fluxes (summed over species and energy) and the total electron precipitation fluxes (summed over energy) are shown in Fig. 1 panels *a* and *b*, respectively.

We note that more recent analysis of both Galileo Energetic Particles Detector (EPD) and Juno Jovian Auroral Distributions Experiment (JADE) and Jupiter Energetic Particle Detector Instruments (JEDI) measurements have provided updated plasma and energetic particle parameters that may affect both the ion and electron precipitation model results of Poppe et al. (2018), Liuzzo et al. (2020). Clark et al. (2016) analyzed a series of energetic ion injection events observed by Galileo EPD, using the charge-state dependent nature of ion dispersion times to infer energetic oxygen and sulfur charge states. This analysis showed that energetic oxygen (E > ~250 keV) possessed charge states of 1+, 2+, and even 3+, while energetic sulfur (E >~500 keV) possessed charge states of 2+, 3+, and 4+. More recently, Kim et al. (2020) have used Juno JADE observations of Jovian ions in the energy range of 100 eV to 100 keV to characterize plasma moments and charge state distributions of H, O, Na, and S. Near Ganymede's orbital distance of ~15 R_J (where R_J=69,911 km is the radius of Jupiter), they found relative ratios of O^+, O^{++}, and O^{+++} of 0.72:0.25:0.03, and relative ratios of S^+, S^{++}, and S^{+++} of 0.19:0.55:0.26. In comparison, Poppe et al. (2018), based primarily on the prior conclusions of Collier and Hamilton (1995), Keppler and Krupp (1996), used only a single oxygen charge state of 2+ and a single sulfur charge state of 3+ in their modeling. Thus, given the range of oxygen and sulfur charge states reported by Clark et al. (2016), Kim et al. (2020), one could reasonably expect variations in the total magnitude and spatial distributions of precipitating oxygen and sulfur to the surface of Ganymede, compared to that presented in Poppe et al. (2018). Despite this, we do not expect the high-level results of Poppe et al. (2018) to significantly change as a result. A full re-modeling and analysis of the role that various charge states (and thus, various charge-to-mass ratios) have on the total ion precipitation to Ganymede is beyond the scope of the present study, but identified as a compelling future investigation.

Most recently, Paranicas et al. (2021) have reported Juno JADE and JEDI observations of proton and electron spectra near Ganymede's orbital distance. When compared to the input proton and electron spectra used in Poppe et al. (2018) and Liuzzo et al. (2020), respectively, we found that the new Juno spectra ranged from nearly equal to ~2 orders-of-magnitude higher in differential flux, depending on the energy. For electrons, the Juno spectrum was approximately one order-of-magnitude higher than the Liuzzo et al. (2020) inputs in the limited range of 10^2–10^3 keV, but otherwise matched closely. For protons, the Juno spectrum was generally one to three orders-of-magnitude higher than that used in Poppe et al. (2018). Thus, based on these observations, we might expect greater precipitation from electrons and protons and therefore greater surface sputtering rates at Ganymede. On the other hand, as acknowledged by Paranicas et al. (2021), the reported Juno spectra are limited in time (i.e., the results were averaged over only a 20-minute time period) and therefore represent only a single 'snapshot' of the environment. High degrees of variability in the electron and ion spectra have been previously reported (e.g., Jun et al. (2005)). Thus, a full quantification of the mean electron, proton, and heavy ion spectra observed by Juno is necessary before making strong conclusions with regards to the total ion and electron precipitation to Ganymede.

2.3. Plasma surface interaction

When the precipitating ions and electrons interact with the surface, they can sputter surface atoms and molecules. To correctly determine the amount of sputtered material, Ganymede's surface composition and surface temperature need to be known. These two properties are not only required to accurately compute the interaction-specific sputter yields, but also to accurately implement the sublimated population in Ganymede's atmosphere. We thus first present the current knowledge on Ganymede's surface composition and surface temperature, before we discuss the current understanding of the H_2O sputter yields for impinging H, O, and S ions as well as electrons.

2.3.1. Ganymede surface water concentration

According to Ligier et al. (2019), >10% to 60% of the surface at latitudes ≤65° consists of water ice, with a clear latitudinal gradient (higher latitude H_2O concentration > lower latitude H_2O concentration), and a hemispherical dichotomy (leading H_2O concentration > trailing H_2O concentration). Since we are interested in the atmosphere originating from the water-ice surface, irrespective of the ice properties, we use Figure 10*b* in Ligier et al. (2019) for the H_2O surface content. Due to constraints placed by the applicability of the photometric model used to correct geometric effects, the water content maps published by Ligier et al. (2019) only present values within 65° of the sub-solar point, i.e., cover Ganymede's surface from −65°N to 65°N in the longitude range 5°W to 310°W. For the missing values in Figure 10*b*, N. Ligier provided us with three estimated average values, one valid for latitudes >65°, one valid for the equatorial longitudinal range 310°W to 5°W, and one valid for the latitudinal range ±(40–60)°N. Fig. 1*c* shows the H_2O surface concentration as implemented in our model.

2.3.2. Ganymede surface temperature

The sub-solar temperature is connected to the constant night-side temperature by a day-side power law (Fray and Schmitt, 2009), which we implement as

$$T(\lambda) = T_{NS} + (T_{SS} - T_{NS}) \cdot \cos(\lambda)^{0.75}, \quad (7)$$

where T_{NS} is the night-side temperature (assumed to be constant at 80 K in our model), T_{SS} is the sub-solar temperature (equal to 150 K in our model), and λ is the solar zenith angle. As almost all previous models mentioned in Section 1.2, we assume the temperature range (80–150) K to be applicable to Ganymede's surface ice, though we would like the reader to keep in mind that 150 K might present an overestimation. The temperature model implemented in our model is presented in Fig. 1*d*.

2.3.3. Sputter yield

The loss rate or sputter yield of H_2O molecules can be organized into two separate regimes, depending on the impacting velocity: Below ~600 km/s, water molecules are ejected by ions via elastic collisions (nuclear sputtering), whereas above (and in the case of electron-sputtering), water molecules are ejected via electronic excitation (electronic sputtering) (see Figure 1 in Vorburger and Wurz (2018)).

For ions, we implement the species- and temperature-dependent water sputter yield curves already presented in several papers (e.g., Shi et al. (1995), Famá et al. (2008), Cassidy et al. (2010), Galli et al. (2018)), and as depicted, for example, in Figure 6 of Teolis et al. (2017). For the angle of incidence, we use 45°, which was shown to be a good approximation for rough surfaces (see e.g., Küstner et al. (1998), Wurz et al. (2007)). For the temperature (80 K–150 K) and energy range (10 eV–10 MeV) of interest, approximate H_2O sputter yields range from 0.01 to 8 for H^+, 1 to 3,000 for O^{n+}, and 1 to 18,000 for S^{+++}.

The efficiency of electrons to sputter H_2O is still largely under debate. Until very recently, laboratory experiments showed that no detectable H_2O was directly sputtered from water ice when irradiated with electrons (see e.g., Galli et al. (2017), Teolis et al. (2017)). Earlier this year, though, Davis et al. (2021) presented experiments where they irradiated water ice at temperatures between 14.5 and 124.5 K with 0.5 keV electrons, from which they inferred a H_2O sputter yield of 0.17. This sputter yield (which is comparable to the proton sputter

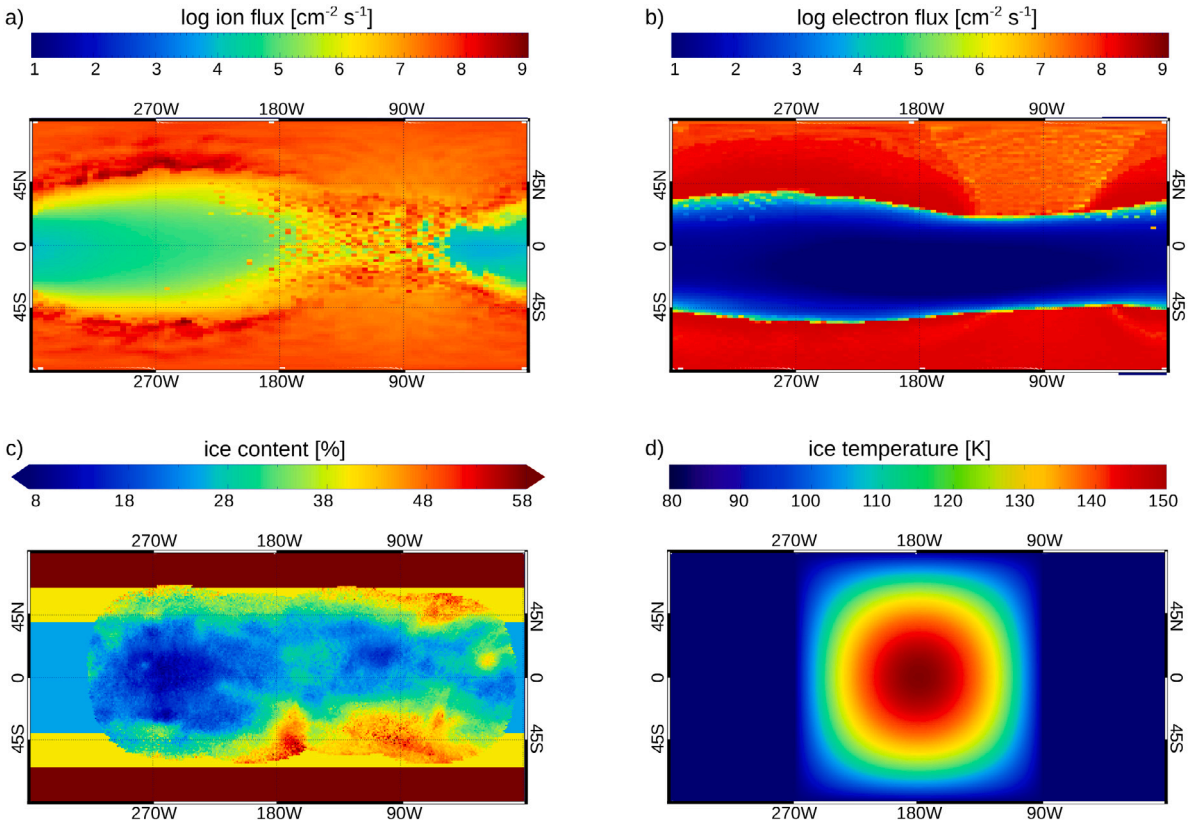

Fig. 1. Model inputs. (a) Ion precipitation fluxes containing all ion species (H^+, O^+, O^{++}, and S^{+++}) from the complete energy range considered (10 eV–10 MeV) taken from Poppe et al. (2018). (b) Electron precipitation map containing fluxes from the complete energy range considered (4.5 keV–100 MeV) obtained from Liuzzo et al. (2020). (c) Ganymede water-ice content taken from Ligier et al. (2019). (d) Surface temperature map based on values provided in Orton et al. (1996), with a constant night-side temperature of 80 K. The trailing hemisphere extends from 180° W to 360° W, the leading hemisphere extends from 0° W to 180° W, the sub-Jovian hemisphere extends from 270° W to 90° W, and the anti-Jovian hemisphere extends from 90° W to 270° W.

yield at 0.5 keV) was not directly measured, though, but rather inferred from the y-intercept of the total mass loss curve. Based on the set of published electron-sputter studies, the H_2O sputter yield of electrons can thus be considered to be either non-existent or to be of similar magnitude as the proton sputter yield. In this study we chose to implement a constant electron sputter yield of 0.17, irrespective of electron energy.

3. Results

In the following two subsections, we will present the results for the sputtered and the sublimated H_2O atmosphere separately, before we combine the results to one total atmosphere in Section 3.3.

3.1. Sputtered atmosphere

3.1.1. Ion sputtered atmosphere

Fig. 2 shows the sputtered H_2O density profiles for thermal H^+, energetic H^+, thermal O^+, energetic O^{++}, and energetic S^{+++}. The left hand side depicts the trailing hemisphere while the right hand side shows the leading hemisphere. In the trailing hemisphere plots Jupiter is located to the left and the Sun to the right, and vice versa in the leading hemisphere plots. The density profiles at radii larger than Ganymede's radius (indicated by the white circle) show a cut through the exosphere in the plane perpendicular to the flow direction and containing the center of Ganymede, while within Ganymede's radius the latitude- and longitude-dependent surface densities are depicted.

If a H_2O molecule re-impacts the surface, the average number of immediate re-ejections it experiences is extremely low (0.01 according to our simulation). This indicates that H_2O immediately freezes out upon returning to the surface, and that it does not form a thermalized atmosphere like O_2 and H_2 do (cf. the sticking fraction presented in Table 1 of Marconi (2007)). The sputtered H_2O surface densities thus strongly resemble the precipitation patterns visible in Fig. 1*a*.

Surface densities are highest for sputtering by oxygen as well as sulfur ions. For these ion species, maximum H_2O surface densities occur near the open-closed field line boundaries and can locally reach $7.6 \cdot 10^{10}$ m^{-3} (thermal O^+), $6.2 \cdot 10^{9}$ m^{-3} (energetic O^{++}), and $2.1 \cdot 10^{10}$ m^{-3} (energetic S^{+++}). The maximum surface densities for hydrogen ion sputtering are by more than a decade lower, reaching up to $8.7 \cdot 10^{8}$ m^{-3} (thermal H^+) and $4.8 \cdot 10^{8}$ m^{-3} (energetic H^+), respectively. Comparison between the thermal and the energetic ion sputtered H_2O density profiles show that while energetic ion sputtered H_2O is strongly enhanced in the polar regions, thermal ion sputtered H_2O also exhibits high densities in the leading equatorial region. As mentioned in the previous paragraph this strongly resembles the patterns in the respective ion precipitation maps. In addition, in the case of both hydrogen and oxygen ions, maximum *local* H_2O surface densities are produced by the precipitating *thermal* ions, while maximum *global* H_2O densities are produced by the impinging *energetic* ions.

Globally, mean equatorial (within 30° latitude of the equator) H_2O surface densities range from $5.6 \cdot 10^{5}$ m^{-3} (thermal and energetic H^+ sputtered) to $9.6 \cdot 10^{8}$ m^{-3} (energetic S^{+++} sputtered), and up to $9.7 \cdot 10^{8}$ m^{-3} (thermal O^+ and energetic O^{++} sputtered). Mean polar (within 15° latitude of the poles) H_2O surface densities are up to a factor of 400 higher, and range from $2.3 \cdot 10^{8}$ m^{-3} (thermal and energetic H^+ sputtered), to $5.1 \cdot 10^{9}$ m^{-3} (thermal O^+ and energetic O^{++} sputtered), and up to $1.1 \cdot 10^{10}$ m^{-3} (energetic S^{+++} sputtered).

Whereas *oxygen* ions produce the highest *local* surface densities (see the beginning of the previous paragraph), it is thus *sulfur* ions that produce the highest *global* surface densities.

Nuclear sputtering imparts more energy to the released particles than electronic sputtering does (see Section 2.1). The scale heights of H_2O molecules sputtered by thermal plasma ions is thus higher (>200 km) than the scale height of H_2O molecules sputtered by energetic ions (~70 km). O^{n+} is the only species that exhibits substantial fluxes in the low energy range, and accordingly is the only species that effectively releases H_2O molecules through nuclear sputtering. The H_2O density profiles for O^{n+} thus exhibit larger scale heights, and decrease more slowly with altitude, than the H_2O density profiles of the other two species. In addition, the sputtered atmosphere is more extended on the anti-Jovian hemisphere than on the sub-Jovian hemisphere, which becomes especially apparent in the plots of energetic H^+, energetic O^{++}, and S^{+++} sputter data. This is due to energetic ions exhibiting lower fluxes onto the sub-Jovian equatorial region than onto the anti-Jovian equatorial region, see Fig. 1*a*.

3.1.2. Electron sputtered atmosphere

Fig. 3 compares the electron sputtered (top) with the total ion sputtered (bottom) H_2O exosphere. This figure shows that the electron sputtered H_2O density profiles are much lower than the total ion sputtered density distributions. Even though the electron precipitation fluxes are higher than the ion precipitation fluxes (see Fig. 1 panels *a* and *b*), the electron sputter yields are too low to efficiently sputter H_2O molecules from Ganymede's icy surface.

As in the case of ion sputtering, the average number of re-ejections a H_2O molecule experiences upon returning to the surface is extremely small (0.01), rendering the electron precipitation pattern clearly visible in the H_2O density profiles. Electron-sputtered H_2O density distributions are quite similar to the density distributions generated by the precipitating energetic protons (energetic H^+ ions), with a local maximum density of $8.2 \cdot 10^8$ m^{-3}, polar average densities of $2.9 \cdot 10^8$ m^{-3}, and equatorial average densities of $4.5 \cdot 10^5$ m^{-3}.

Electrons exclusively sputter through electronic sputtering, imparting less energy onto the H_2O molecules than nuclear sputtering would. The density profiles associated with electron sputtering thus exhibit scale heights similar to the scale heights for sputtering by energetic ions mentioned above.

Finally, according to our simulation, out of all lost particles ~99% are lost to surface sticking, while ~1% escapes Ganymede's atmosphere and ~0.1% is lost to ionization and dissociation. In the case of ion sputtering, ~93% are lost due to surface sticking, ~7% escape, and <1% are lost due to ionization and dissociation. Fewer particles are thus lost to gravitational escape in the electron sputtered atmosphere than in the ion sputtered atmosphere. This can be explained by the fact that electronic sputtering is a less energetic process than nuclear sputtering, with the latter only occurring for ions, as discussed in Section 2.1.

3.2. Sublimated atmosphere

The sublimation flux is strongly temperature dependent (cf. Fray and Schmitt (2009)). In addition, the release process provides very low energy particles to the atmosphere, resulting in the atmosphere being confined to the very near-surface vicinity. The H_2O sublimated atmosphere thus looks very different from the sputtered atmosphere.

In Fig. 4 we present the sublimated H_2O atmosphere, again for the trailing and the leading hemispheres separately. As before, in the left hand plots the Sun is located to the right, whereas in the right hand plots the Sun is located to the left. Note that due to the smaller scale height of sublimated particles compared to sputtered particles (26–49 km compared to 70–260 km, respectively), we present these simulations with increased spatial resolution (23 km instead of >92 km), and show a smaller extent of the atmosphere (0–5,000 km instead of 0–3 R_G). In addition, due to the much higher surface densities (see next paragraph), the colorbar is extended to contain 5 more orders of magnitude than Figs. 2 and 3 do.

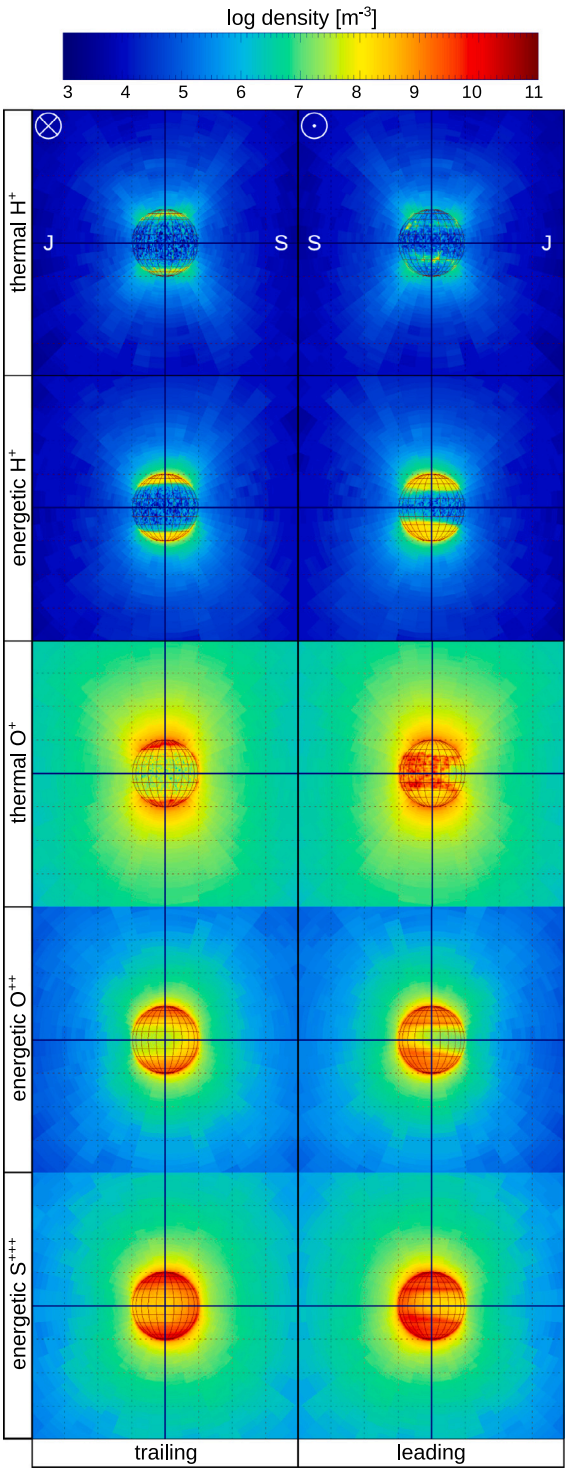

Fig. 2. Thermal H^+, energetic H^+, thermal O^+, energetic O^{++}, and energetic S^{+++} sputtered H_2O density distributions. The panels on the left show the trailing hemispheres, whereas the panels on the right show the leading hemisphere, i.e., the Jovian co-rotating plasma moves into (out of) the trailing (leading) plane as indicated in the top row. Also in the top row, the positions of the Sun (S) and Jupiter (J) are indicated.

The sublimated H_2O surface densities reach much higher values than the sputtered H_2O surface densities. At the sub-solar point, the

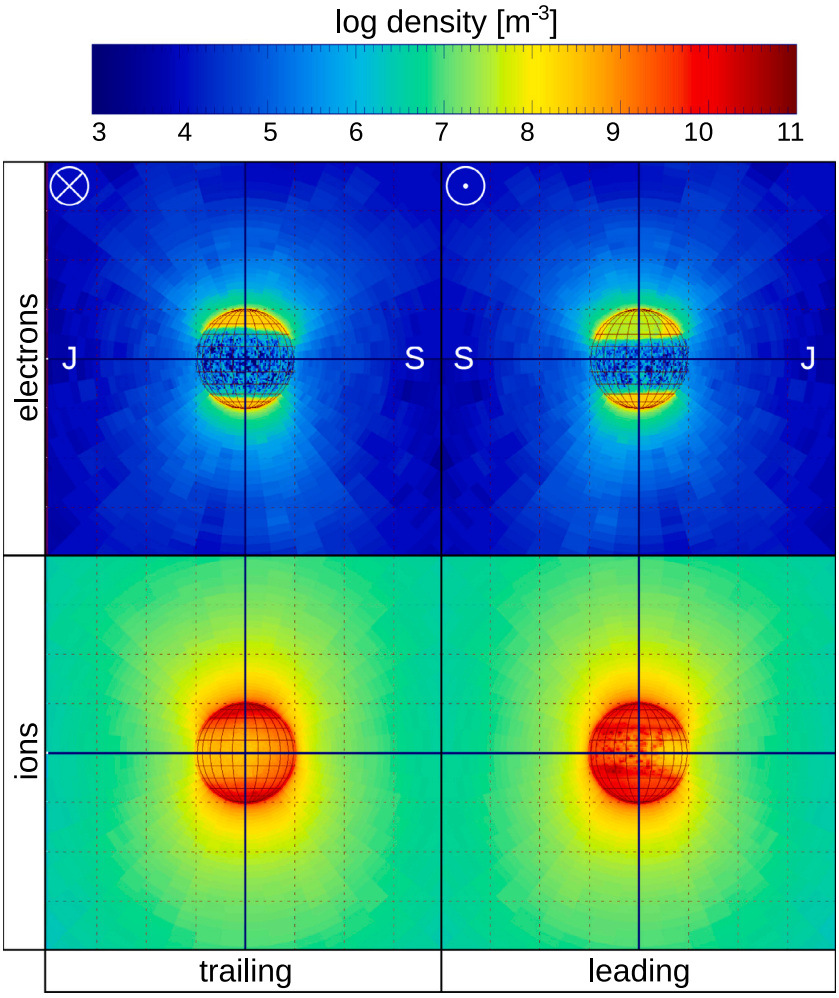

Fig. 3. Electron (top) and total ion (bottom) sputtered H_2O density profiles. The profiles on the left show the trailing hemispheres, whereas the profiles on the right show the leading hemisphere, i.e., the Jovian co-rotating plasma moves into (out of) the trailing (leading) plane as indicated in the top row. Also in the top row, the positions of the Sun (S) and Jupiter (J) are indicated.

surface density is $4.0 \cdot 10^{15}$ m^{-3}, more than four orders of magnitude higher than the maximum sputtered H_2O surface density. Due to the strong temperature dependence (the H_2O surface concentration influence is minor in comparison), the surface densities decrease rapidly with solar zenith angle, though. At the terminator, surface densities have already decreased to $8.2 \cdot 10^2$ m^{-3}. A surface density of $8 \cdot 10^{10}$ m^{-3}, the maximum value in the total sputtered density profiles, is reached at distances of ~63° from the sub-solar point.

In radial direction, the sublimated H_2O density profiles also decrease rapidly, with sublimated molecules only reaching altitudes of a few hundred kilometers. Sublimation thus dominates the H_2O surface densities up to a solar zenith angle of ~60° and up to altitudes of a few hundred kilometers. At larger distances from the sub-solar point and/or higher altitudes it is the sputtered molecules that dominate.

3.3. Total atmosphere

Fig. 5 shows the total (sputtered and sublimated) H_2O density distribution, with the larger spatial extents of Figs. 2 and 3, and with the extended colorbar from Fig. 4. In these plots, the approximate region where sublimation dominates is highlighted by the gray outlines. The dominance of sublimation over sputtering is quite pronounced, but also well-confined to the vicinity (both in longitude/latitude and in altitude) of the sub-solar point.

Fig. 6 presents line density profiles for each process investigated. Figs. 2 through 5 exhibit distinct differences in the individual hemispheres, hence the line density profiles are shown separately for the four hemispheres (trailing, leading, sub-Jovian, and anti-Jovian) and two regions of interest (equator and poles). In this figure the equatorial plot depicts average densities from within ±45 ° of the equator whereas the polar plot depicts average densities from latitudes higher than ±45 °. Note that with one million particles a dynamic range of $\sim 10^6$ can be covered. For the sublimated density profiles, we therefore had to extrapolate densities for altitudes $\gtrsim$700 km (cf. Fig. 6).

The line density profiles confirm and emphasize conclusions presented earlier, and provide easier to read density values. Sublimated H_2O exhibits the highest surface densities by up to almost 4 orders of magnitudes, and dominates the density profiles up to altitudes of ~600 km, except for on the night-side hemisphere (sub-Jovian hemisphere here), where sputtering is always the dominant process. In the polar regions, where temperatures are smaller and precipitation fluxes are higher, the altitude at which sublimation dominates is approximately cut in half, and the sublimated surface density dominance is also reduced to approximately one order of magnitude. Between 100 and 200 km, H_2O molecules sputtered by thermal O^+ start to dominate over the molecules sputtered by energetic S^{+++}. As mentioned previously, this is due to oxygen being the only ion species that contains considerable fluxes in the low energy range. That H_2O molecules

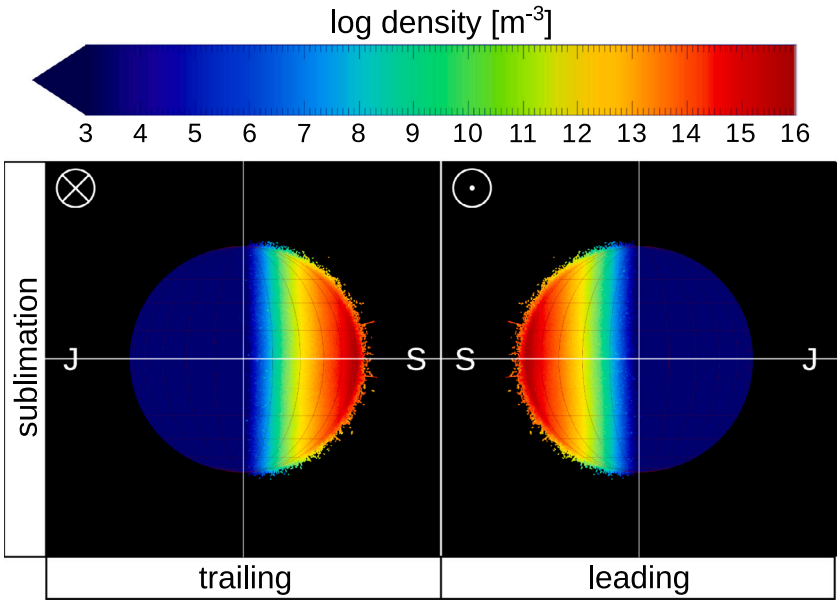

Fig. 4. Sublimated H_2O density profiles. The left hand side shows the trailing hemisphere while the right hand side shows the leading hemisphere. Note that in this Figure the colorbar is different from the colorbar used in Figs. 2 and 3. The positions of the Sun (S) and Jupiter (J), as well as the plasma flow (not relevant here), are indicated.

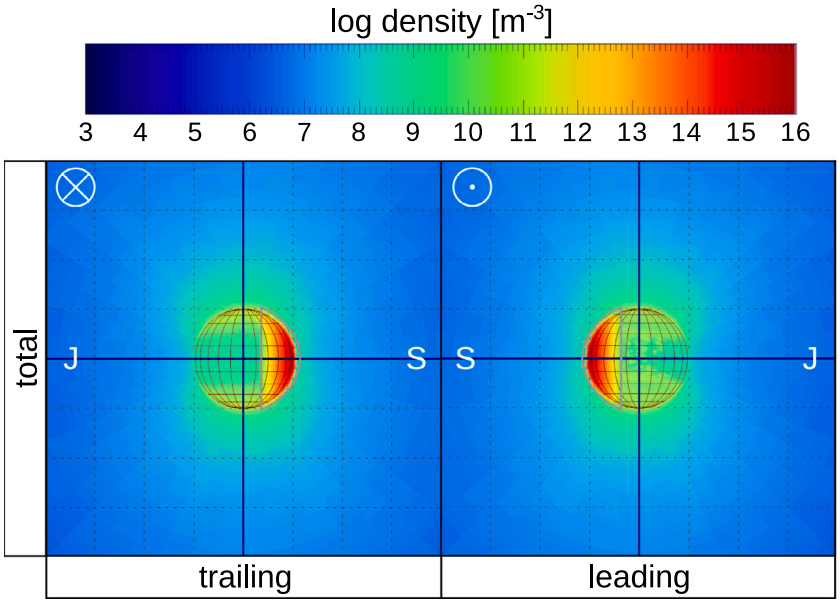

Fig. 5. Overall H_2O density profiles. As in the other figures, the trialing hemisphere is shown on the left side, whereas the leading hemisphere is shown on the right side, i.e., the Jovian co-rotating plasma moves into (out of) the trailing (leading) plane as indicated. The gray outlines indicate the approximate area where sublimation dominates. The positions of the Sun (S) and Jupiter (J) are also indicated.

sputtered by thermal ions exhibit higher scale heights than molecules sputtered by energetic particles is also visible in the H^+ and O^{n+} density profiles, where in both cases the thermal profiles are shallower than the energetic counterparts. Finally, note that the electron sputter profiles are very similar to the energetic proton (energetic H^+) sputter profiles, both of which produce the lowest densities.

An overview of the importance of the different processes is also given in Table 2, where we present for each process investigated the total number of particles that are present in the atmosphere due to said process, the release rates, the scale heights, the maximum and mean surface densities, and the maximum and mean column densities. Overall, sublimation delivers the largest amount of particles to the atmosphere, more than 3 orders of magnitude more than sputtering does. The scale height of the sublimated particles is lower than the scale height of the sputtered particles, resulting in the dominance of the sublimated H_2O particles being confined to near-surface altitudes. Further out, or at higher solar zenith angles, it is the H_2O molecules sputtered by thermal O^+ and energetic S^{+++} that dominate the atmosphere. Sputtering by H^+ and electrons are minor processes in comparison.

Finally, Fig. 7 presents the H_2O radial column densities associated with each process obtained by radially integrating the densities from the surface out to the Hill radius. Note that the colorbar was chosen so that the morphologies are clearly visible in the sputter-related plots. The maximum value in the colorbar is by four orders of magnitude

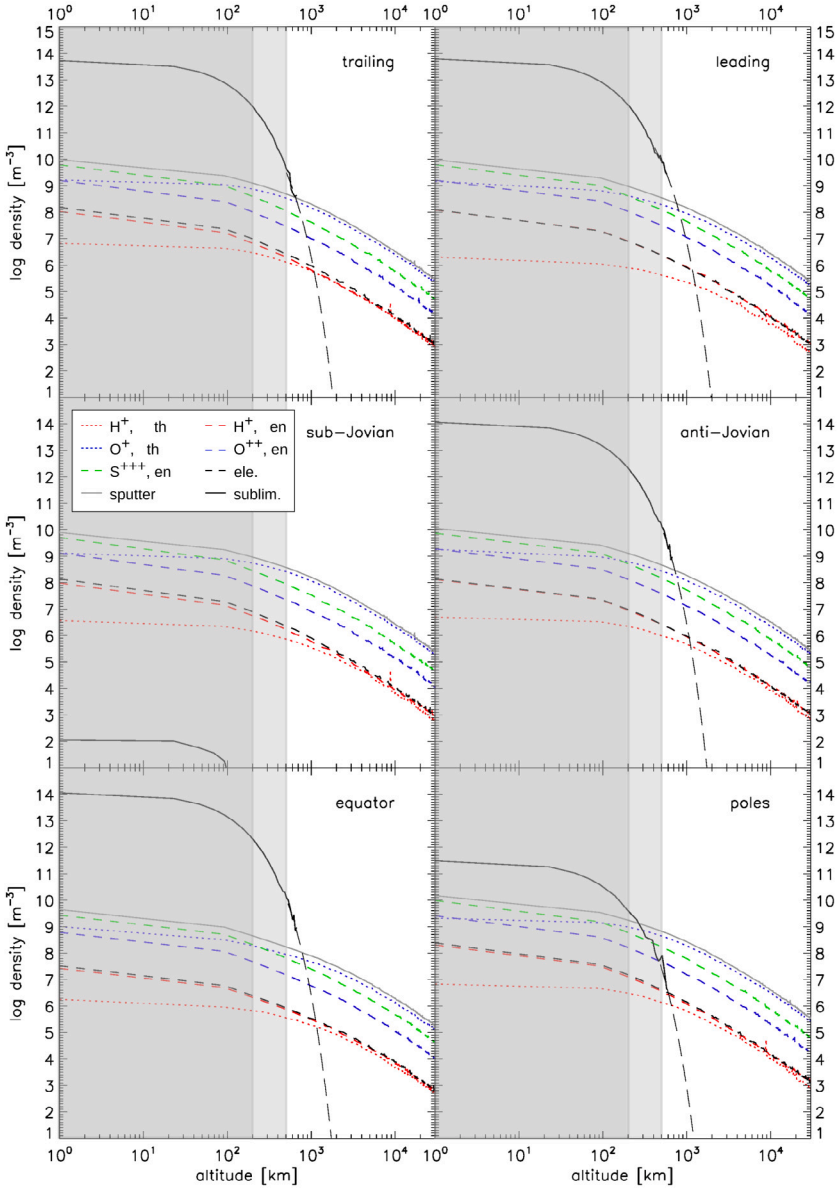

Fig. 6. H_2O line density profiles for the four hemispheres (trailing, leading, sub-Jovian, and anti-Jovian) as well as two latitude regions of interest (equator and poles). The color-coding is as follows: red dotted = thermal H^+ sputtered, red dashed = energetic H^+ sputtered, blue dotted = thermal O^+ sputtered, blue dashed = energetic O^{++} sputtered, green dashed = energetic S^{+++} sputtered, black dashed = electron sputtered, gray solid = total sputtered, black solid = sublimated, and black long dashed = extrapolated sublimated. The light (dark) gray background denotes the altitude inaccessible to JUICE during its circular (elliptical) orbits. (For interpretation of the references to color in this figure legend, the reader is referred to the web version of this article.)

Table 2
Amount of particles present in the atmosphere, release rates (R_{rel}), scale heights (H), maximum and mean surface densities (N_0), and maximum and mean column densities (NC), for each simulated process.

	# particles [–]	R_{rel} [s^{-1}]	H [km]	N_0 [m^{-3}]		NC [m^{-2}]	
				max	mean	max	mean
H^+, th	$5.6 \cdot 10^{26}$	$1.2 \cdot 10^{23}$	257	$1.3 \cdot 10^{8}$	$4.3 \cdot 10^{6}$	$2.5 \cdot 10^{13}$	$2.0 \cdot 10^{12}$
H^+, en	$1.4 \cdot 10^{27}$	$1.7 \cdot 10^{24}$	70	$4.1 \cdot 10^{8}$	$1.1 \cdot 10^{8}$	$5.5 \cdot 10^{13}$	$1.5 \cdot 10^{13}$
O^+, th	$1.4 \cdot 10^{29}$	$3.7 \cdot 10^{25}$	208	$1.6 \cdot 10^{10}$	$1.6 \cdot 10^{9}$	$4.0 \cdot 10^{15}$	$6.3 \cdot 10^{14}$
O^{++}, en	$2.2 \cdot 10^{28}$	$2.6 \cdot 10^{25}$	70	$4.5 \cdot 10^{9}$	$1.6 \cdot 10^{9}$	$6.1 \cdot 10^{14}$	$2.2 \cdot 10^{14}$
S^{+++}, en	$8.9 \cdot 10^{28}$	$1.0 \cdot 10^{26}$	70	$1.6 \cdot 10^{10}$	$6.2 \cdot 10^{9}$	$2.2 \cdot 10^{15}$	$8.4 \cdot 10^{14}$
electrons	$1.6 \cdot 10^{27}$	$2.0 \cdot 10^{24}$	70	$5.4 \cdot 10^{8}$	$1.4 \cdot 10^{8}$	$7.2 \cdot 10^{13}$	$1.9 \cdot 10^{13}$
sum sputter	$2.6 \cdot 10^{29}$	$1.7 \cdot 10^{26}$	–	$2.6 \cdot 10^{10}$	$9.6 \cdot 10^{9}$	$5.7 \cdot 10^{15}$	$1.7 \cdot 10^{15}$
sublimation	$4.8 \cdot 10^{32}$	$9.1 \cdot 10^{29}$	47	$2.9 \cdot 10^{15}$	$5.8 \cdot 10^{13}$	$1.7 \cdot 10^{20}$	$3.5 \cdot 10^{18}$

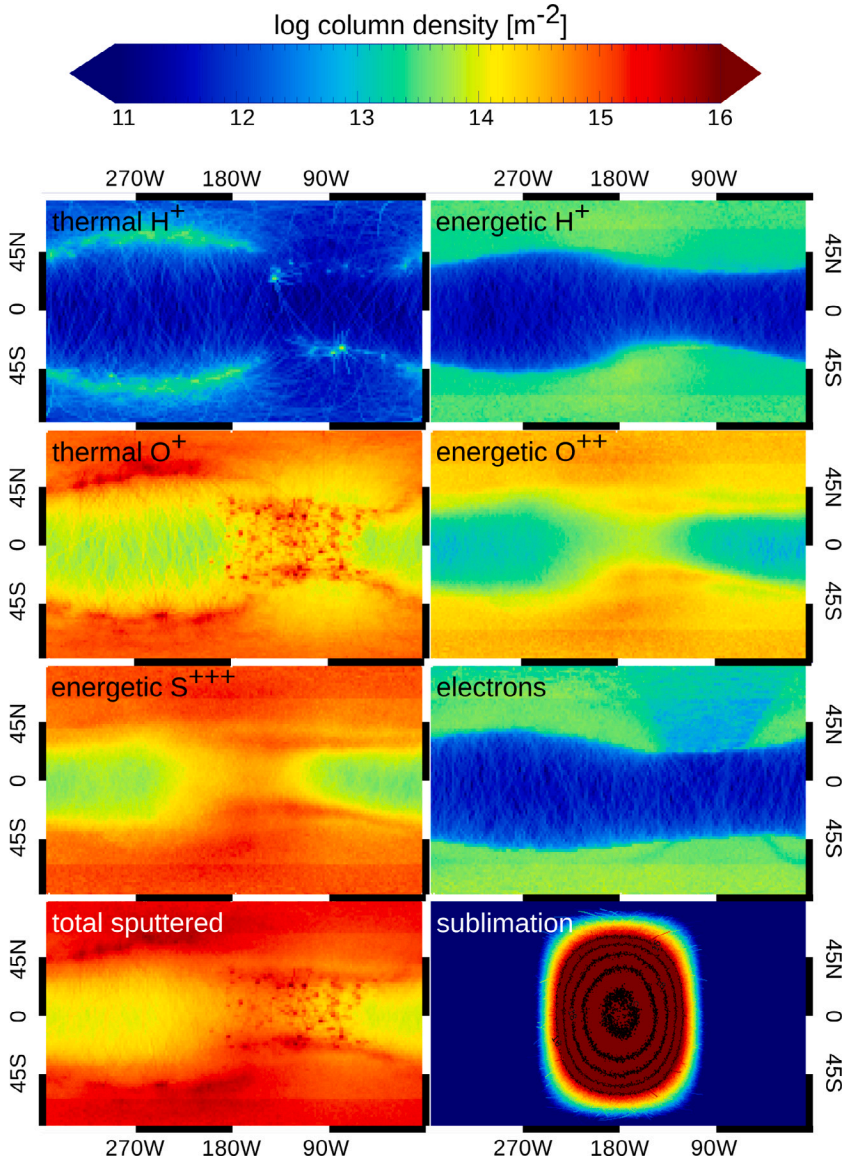

Fig. 7. Radial H_2O column densities. Top row left: thermal H^+ sputtered, top row right: energetic H^+ sputtered, second row left: thermal O^+ sputtered, second row right: energetic O^{++} sputtered, third row left: energetic S^{+++} sputtered, third row right: electron sputtered, bottom row left: sum of all sputtered, bottom row right: sublimated. For the sublimated column densities contour lines at 10^{16}, 10^{17}, 10^{18}, 10^{19}, and 10^{20} m^{-2} are shown.

lower than what would be required to correctly depict sublimated column densities. We thus also show contour lines at 10^{16}, 10^{17}, 10^{18}, 10^{19}, and 10^{20} m^{-2} in the last panel.

The column densities clearly resemble the precipitation maps. Again, this is due to the high sticking probability (0.99) of H_2O. The sputtered H_2O column densities exhibit the highest values in the polar region and in the equatorial region of the leading hemisphere, being mostly the result of the thermal O^+ and the energetic S^{+++} sputtering. The column densities associated with sublimation clearly dominate most of the sunlit hemisphere, but are negligible on the night-side.

4. Discussion & conclusion

Our model simulates Ganymede's H_2O atmosphere *ab initio*, i.e., according to the current best understanding of the underlying physics without applying any scaling factors. Our results, which are presented in very high detail, reinforce the consensus reached about the properties of Ganymede's water atmosphere, which can be thought of as consisting of two parts, a sublimated water atmosphere dominating up to a solar zenith angle of ~60° and up to altitudes of ~600 km, and a sputtered atmosphere dominating elsewhere. The sublimated H_2O atmosphere exhibits surface densities up to several 10^9 cm^{-3}, whereas the sputtered H_2O atmosphere exhibits surface densities on the order of ~10^4 cm^{-3}, i.e., values approximately five order of magnitudes lower. As mentioned, though, the region where the sublimated H_2O atmosphere prevails is strongly confined by the strong temperature-dependence of, and the low scale-height associated with, the release mechanism. Note that in our simulation, we modeled one specific position along Ganymede's orbit (where the sub-solar point coincides with the anti-Jovian sub-point). For a different Sun-plasma angle, the sublimated atmosphere would be shifted to the appropriate longitudes (and the sputter yields would change marginally), but the results mentioned above would still hold true.

Roth et al. (2021) recently presented first observational evidence in support of sublimated H_2O in Ganymede's atmosphere. In their observations, the sunlit hemisphere coincides once with the trailing hemisphere

and once with the leading hemisphere. In our simulation, the sub-solar point coincides with the anti-Jovian sub-point. Through modeling, Roth et al. (2021) derive maximum sublimated H_2O surface densities of 1.2 $\cdot 10^9$ cm^{-3} (sunlit trailing hemisphere) & 2.0 $\cdot 10^8$ cm^{-3} (sunlit leading hemisphere), and column densities on the order of several 10^{15} cm^{-2}. Our simulations result in maximum sublimated H_2O surface densities of 4.8 $\cdot 10^9$ cm^{-3} and maximum column densities of 2.4 $\cdot 10^{16}$ cm^{-2}. Our values are thus slightly higher than the values derived by Roth et al. (2021). The apparent slight over-estimation in our simulations can be explained by the following two facts. First of all, the surficial water content in the anti-Jovian equatorial region is higher than the content in both the trailing and the leading equatorial region (see Fig. 1*c*). Decreasing the water content to the values observed on the trailing and the leading hemisphere would lower the maximum modeled surface densities down to ~2 $\cdot 10^9$ cm^{-3}. Secondly, Roth et al. (2021) state that they assume maximum surface temperatures of 148 K at the trailing hemisphere and 142 K at the leading hemisphere. As mentioned before, our maximum surface temperature of 150 K might present a slight over-estimation of the true maximum surface temperature. If the maximum surface temperatures truly were in the range (142–148) K, based on vapor-pressure considerations, our surface densities would be lowered to values of (5.1–29)$\cdot 10^8$ cm^{-3}. Combining both effects results in maximum sublimated H_2O surface densities of 1.2 $\cdot 10^9$ cm^{-3} (trailing hemisphere) and 3.7 $\cdot 10^8$ cm^{-3} (leading hemisphere), values in extremely good agreement with the Roth et al. (2021) observations.

Comparison with previously published modeling efforts on Ganymede's atmosphere shows that our results in general agree well with, but are slightly higher than, the results obtained by other modeling groups. Previously reported maximum sublimated H_2O release fluxes are on the order of (1–10)$\cdot 10^{13}$ cm^{-2}s^{-1} (with the exception of the 'low sublimation case' presented by Leblanc et al. (2017)). We compute a sublimation flux of 7.2 $\cdot 10^{13}$ cm^{-2}s^{-1} at the sub-solar point, which fits perfectly within this range. For sputtering, most previously published models assume a H_2O sputter release flux of 1.8 $\cdot 10^8$ cm^{-2}s^{-1}, except Leblanc et al. (2017), who derives sputter fluxes one to two orders of magnitude higher. Our value of 2.9 $\cdot 10^8$ cm^{-2}s^{-2} is 1.6 times higher than the 1.8 $\cdot 10^8$ cm^{-2}s^{-1}. The fact that our fluxes are slightly higher than previously computed sputter fluxes is due to the fact that our study not only considers all relevant ion species (H^+, O^+, O^{++}, S^{+++}) plus electrons, but also because the incorporated precipitation fluxes cover the largest energy range considered in Ganymede atmosphere modeling studies to date (10 eV–100 MeV). Column densities have only been presented sparsely for previously published models. Marconi (2007) and Leblanc et al. (2017) derive maximum sublimated H_2O column densities on the order of 1 $\cdot 10^{16}$ cm^{-2}, while our maximum sublimated H_2O column density is equal to 1.7 $\cdot 10^{16}$ cm^{-2}. For sputtering, Marconi (2007) publishes maximum column densities of 2 $\cdot 10^{11}$ cm^{-2}, whereas Leblanc et al. (2017), who uses sputter fluxes one to two orders of magnitude higher than the other modelers, derives maximum sputtered H_2O column densities of a few 10^{13} cm^{-2}. Our maximum sputtered H_2O column density of 5.7 $\cdot 10^{11}$ cm^{-3} is almost three times higher than the maximum Marconi (2007) column density but, like Marconi (2007), two orders of magnitude lower than the Leblanc et al. (2017) values. Finally, our computed neutral escape rate of 8.5 $\cdot 10^{24}$ s^{-1} is well in the range of previously published H_2O neutral escape rates of (1–10)$\cdot 10^{24}$ s^{-1}.

Out of the four sputter agents investigated (H^+, O^{n+}, S^{+++}, and electrons), it is the impinging oxygen and sulfur ions that stimulate the largest fraction of sputtered H_2O. Protons (H^+) and electrons, which result in very similar sputtered H_2O density profiles, deliver only about half a percent of the total sputtered molecules. Moreover, as mentioned earlier, the efficiency with which electrons sputter water molecules is still strongly debated. The electron sputter yield used herein corresponds to the highest yield published to date. Thus even the mentioned half percent might present an overestimation. Oxygen is the only ion species that exhibits substantial fluxes in the thermal energy range, and is accordingly responsible for the extended ($\gtrsim 1$ R_G) atmosphere. Out of all the variables included in this model for sputtering, it is the precipitation flux that defines the structure of the sputtered atmosphere. Neither the water content nor the surface temperature affect the flux of sputtered water molecules enough to have a visible effect in the atmospheric density profiles. In future modeling efforts, omission of the later two parameters can thus be justified for Ganymede's sputtered atmosphere. This is not true for sublimation, where temperature is by far the dominating parameter determining the structure of the created atmosphere.

The trailing/leading hemisphere dichotomy that can be observed in the precipitation fluxes is also visible in the sputtered atmosphere, up to altitudes of at least ~1000 km. The same is true for the high precipitation rates to the polar regions: Up to altitudes of a few thousand km the sputtered atmosphere exhibits higher densities in the polar regions as well. At even higher altitudes, the atmosphere is close to uniform.

Most water molecules that are released into Ganymede's atmosphere return to the surface where they immediately freeze out. Out of the ~9 $\cdot 10^{29}$ sublimated H_2O molecules that are fed to the atmosphere every second, only about ~8 $\cdot 10^{24}$ molecules s^{-1} are lost to space as escaping neutrals according to our simulations. The calculated ion loss rates are by almost a factor 10 higher (~2 $\cdot 10^{26}$ ions s^{-1}), with the ions being picked-up by the electro-magnetic field, which may result in mass loading of the Jovian plasma.

In our study we omitted the inclusion of an ionosphere. The presence of a dense ionosphere could potentially lower the atmospheric density profiles by reducing the plasma precipitation and by providing an additional loss mechanism (charge-exchange). On the other hand, an ionosphere could increase the atmospheric density profiles by providing an additional source (ionospheric sputtering). To date, the ionosphere of Ganymede is still poorly constrained. The only observational constraints available come from the Galileo mission. According to the measurements analyzed by Frank et al. (1997), Kliore (1998), Eviatar et al. (2001), the ionosphere has an upper limit of 4,000 cm^{-3} and is mainly composed of oxygen and hydrogen, which Carnielli et al. (2019) modeled to be primarily O_2^+ ions, followed by O^+, H_2^+, and H_2O^+. Based on a later study by the same authors, ionospheric ions contribute at least 10% to the sputtering rate (Carnielli et al., 2020b). In that case our results provide a slight underestimation of the sputtered atmosphere, though given the uncertainties in the other model aspects (e.g., plasma precipitation, sputter yield, surface composition), this potential underestimation does not seem substantial. As mentioned above, an ionosphere, if dense enough, could on the other hand lower the precipitation flux and at the same time lower the atmospheric density by acting as a sink mechanism. Plainaki et al. (2015) estimate the ionosphere-related loss rate to be up to 10 times higher than the loss rates due to photons and electrons combined. Both of these effects would counteract the additional source provided by ionospheric sputtering. The overall influence an ionosphere might have on the atmosphere thus still remains an open question and should further be investigated.

Fig. 7 shows the radial column density for each location on the surface for each process separately. This figure shows that if the illuminated hemisphere is observed spectroscopically from afar (e.g. by observing Lyman-α and oxygen emission lines), it is the sublimated atmosphere that dominates the signal. On the night-side, on the other hand, it is mainly the sputtered atmosphere that is observed spectroscopically. As mentioned earlier, electrons, which were modeled to be an important contributor for O_2 and H_2 in Europa's sputtered atmosphere, are not a major contributor to the H_2O sputtered atmosphere of Ganymede. If it is electron-excited line emission that are observed, though, it is the electron-atmosphere interaction that becomes the most important interaction process. Whereas electrons are thus not necessarily required to model the generation of Ganymede's sputtered atmosphere, they are highly relevant when it comes to the spectral observability of the atmosphere.

For *in-situ* atmospheric measurements (e.g., by mass-spectrometers), it is mainly the sputtered atmosphere that is probed, unless the instrument is brought to altitudes lower than ~600 km during close flybys. Furthermore, even if an *in-situ* instrument is in a low (<600 km) polar orbit, it will only spend part of its orbit on the sun-lit hemisphere, where it can measure the sublimated atmosphere. To correctly predict *in-situ* measurements, and to correctly interpret *in-situ* data, a thorough understanding of the sputtered atmosphere is thus crucial. JUICE, the ESA mission to Jupiter and its icy moons Grasset et al. (2013), currently plans on observing Ganymede first from an elliptical orbit with a pericenter at 200 km and an apocenter at 10,000 km, and in its final stage from a ~500 km circular orbit. NIM, the Neutral and Ion Mass spectrometer, which is part of the Particle Environment Package (PEP) onboard JUICE, will measure the neutral and ion composition of Ganymede's atmosphere and ionosphere (Föhn et al., 2021). The region accessible to NIM is denoted by the white background in Fig. 6, whereas the region inaccessible to NIM during its circular (elliptical) orbits is indicated by the light (dark) gray background. NIM will measure the sputtered atmosphere most of the time during the elliptical orbits, except for the times around closest approach, if the closest approach is near the sub-solar region. During the ~500 km circular orbits NIM will measure the sublimated atmosphere at maximum during one third of the orbit, and the sputtered atmosphere for at least two thirds of the orbit. The measurements of each individual orbit will thus allow a direct comparison between the sputtered and the sublimated atmosphere. The data-set of the complete mission will provide us with a wide range of different observations with respect to solar time, plasma flow, and surface location below the spacecraft. This will allow for a very thorough understanding of the two atmospheric populations (sputtered and sublimated) in Ganymede's atmosphere and the different parameters that influence these atmospheric populations.

Since Ganymede is the only moon that possesses a substantial, intrinsic magnetic field, the generation mechanism of the moon's atmosphere is unique: this magnetic field shapes the precipitation patterns of ions and electrons, which in turn defines the structure of the sputtered H_2O atmosphere. The resulting structure of the atmosphere is visible up to altitudes of a few thousand km. In-situ measurements of the sputtered atmosphere at high (> few hundred kilometer) altitudes, where the sublimated atmosphere has already vanished, will thus reveal important clues not only on the atmosphere itself, but also about Ganymede's magnetic field.

Acknowledgments

A. V. and S. F. acknowledge support from the Swedish National Space Agency (SNSA), grant 179/18. S. F. also acknowledges supports from SNSA grant 115/18 and the Swedish Research Council (VR) grant 2018-03454. N. Ligier kindly provided us estimated values for the missing regions in his Figure 10 *b*. We also acknowledge the fruitful discussions with R. E. Johnson on energy distributions of sputtered H2O molecules. For the JUICE trajectories we used CREMA 5 (https://juicesoc.esac.esa.int/tm/?trajectory=CREMA_5_0).

References

Alday, J., Roth, L., Ivchenko, N., Retherford, K.D., Becker, T.M., Molyneux, P., Saur, J., 2017. New constraints on Ganymede's hydrogen corona: Analysis of Lyman-α emissions observed by HST/STIS between 1998 and 2014. Planet. Space Sci. 148, 35–44. http://dx.doi.org/10.1016/j.pss.2017.10.006.

Barth, C.A., Hord, C.W., Stewart, A.I.F., Pryor, W.R., Simmons, K.E., McClintock, W.E., Ajello, J.M., Naviaux, K.L., Aiello, J.J., 1997. Galileo ultraviolet spectrometer observations of atomic hydrogen in the atmosphere of Ganymede. Geophys. Res. Lett. 24 (17), 2147–2150. http://dx.doi.org/10.1029/97GL01927.

Brown, M.E., Bouchez, A.H., 1999. Observations of Ganymede's visible aurorae. In: Bulletin of the American Astronomical Society. 31. p. 1183.

Calvin, W.M., Clark, R.N., 1991. Modeling the reflectance spectrum of callisto 0.25 to 4.1 μm. Icarus 89 (2), 305–317. http://dx.doi.org/10.1016/0019-1035(91)90180-2.

Calvin, W.M., Clark, R.N., Brown, R.H., Spencer, J.R., 1995. Spectra of the icy Galilean satellites from 0.2 to 5 μm: A compilation, new observations, and a recent summary. J. Geophys. Res. 100 (E9), 19041–19048. http://dx.doi.org/10.1029/94JE03349.

Carlson, R., Smythe, W., Baines, K., Barbinis, E., Becker, K., Burns, R., Calcutt, S., Calvin, W., Clark, R., Danielson, G., Davies, A., Drossart, P., Encrenaz, T., Fanale, F., Granahan, J., Hansen, G., Herrera, P., Hibbitts, C., Hui, J., Irwin, P., Johnson, T., Kamp, L., Kieffer, H., Leader, F., Lellouch, E., Lopes-Gautier, R., Matson, D., McCord, T., Mehlman, R., Ocampo, A., Orton, G., Roos-Serote, M., Segura, M., Shirley, J., Soderblom, L., Stevenson, A., Taylor, F., Torson, J., Weir, A., Weissman, P., 1996. Near-infrared spectroscopy and spectral mapping of jupiter and the galilean satellites: Results from Galileo's initial orbit. Science 274 (5286), 385–388. http://dx.doi.org/10.1126/science.274.5286.385.

Carnielli, G., Galand, M., Leblanc, F., Leclercq, L., Modolo, R., Beth, A., Huybrighs, H.L.F., Jia, X., 2019. First 3D test particle model of Ganymede's ionosphere. Icarus 330, 42–59.

Carnielli, G., Galand, M., Leblanc, F., Modolo, R., Beth, A., Jia, X., 2020a. Constraining Ganymede's neutral and plasma environments through simulations of its ionosphere and Galileo observations. Icarus 113691.

Carnielli, G., Galand, M., Leblanc, F., Modolo, R., Beth, A., Jia, X., 2020b. Simulations of ion sputtering at Ganymede. Icarus 351, 113918.

Cassidy, T., Coll, P., Raulin, F., Carlson, R., Johnson, R., Loeffler, M., Hand, K., Baragiola, R., 2010. Radiolysis and photolysis of icy satellite surfaces: Experiments and theory. Space Sci. Rev. 153, 299–315. http://dx.doi.org/10.1007/s11214-009-9625-3.

Cassidy, T., Johnson, R., 2005. Monte Carlo Model of sputtering and other ejection processes within a regolith. Icarus 176 (2), 499–507. http://dx.doi.org/10.1016/j.icarus.2005.02.013.

Clark, G., Mauk, B.H., Paranicas, C., Kollmann, P., Smith, H.T., 2016. Charge states of energetic oxygen and sulfur ions in Jupiter's magnetosphere. J. Geophys. Res. Space Phys. 121 (3), 2264–2273.

Collier, M.R., Hamilton, D.C., 1995. The relationship between kappa and temperature in energetic ion spectra at jupiter. Geophys. Res. Lett. 22 (3), 303–306. http://dx.doi.org/10.1029/94GL02997.

Cooper, J.F., Johnson, R.E., Mauk, B.H., Garrett, H.B., Gehrels, N., 2001. Energetic ion and electron irradiation of the Icy Galilean satellites. Icarus 149, 133–159. http://dx.doi.org/10.1006/icar.2000.6498.

Davis, M.R., Meier, R.M., Cooper, J.F., Loeffler, M.J., 2021. The contribution of electrons to the sputter-produced O_2 exosphere on Europa. Astrophys. J. Lett. 908 (2), L53. http://dx.doi.org/10.3847/2041-8213/abe415.

Domingue, D.L., Lane, A.L., Beyer, R.A., 1998. IUE's detection of tenuous SO_2 frost on Ganymede and its rapid time variability. Geophys. Res. Lett. 25 (16), 3117–3120. http://dx.doi.org/10.1029/98GL02386.

Eviatar, A., Strobel, D.F., Wolven, B.C., Feldman, P.D., McGrath, M.A., Williams, D.J., 2001. Excitation of the ganymede ultraviolet Aurora. Astrophys. J. 555 (2), 1013–1019. http://dx.doi.org/10.1086/321510.

Famá, M., Shi, J., Baragiola, R.A., 2008. Sputtering of ice by low-energy ions. Surf. Sci. 602, 156–161. http://dx.doi.org/10.1016/j.susc.2007.10.002, URL www.sciencedirect.com.

Fatemi, S., Poppe, A.R., Khurana, K.K., Holmström, M., Delory, G.T., 2016. On the formation of Ganymede's surface brightness asymmetries: Kinetic simulations of Ganymede's magnetosphere. Geophys. Res. Lett. 43 (10), 4745–4754. http://dx.doi.org/10.1002/2016GL068363.

Feldman, P.D., McGrath, M.A., Strobel, D.F., Moos, H.W., Retherford, K.D., Wolven, B.C., 2000. HST/STIS ultraviolet imaging of polar aurora on Ganymede. Astrophys. J. 535 (2), 1085–1090. http://dx.doi.org/10.1086/308889.

Föhn, M., Galli, A., Vorburger, A., Tulej, M., Lasi, D., Riedo, A., Fausch, R.G., Althaus, M., Brüngger, S., Fahrer, P., Gerber, M., Lüthi, M., Munz, H.P., Oeschger, S., Piazza, D., Wurz, P., 2021. Description of the mass spectrometer for the jupiter icy moons explorer mission. In: 2021 IEEE Aerospace Conference (50100). pp. 1–14. http://dx.doi.org/10.1109/AERO50100.2021.9438344.

Frank, L.A., Paterson, W.R., Ackerson, K.L., Bolton, S.J., 1997. Outflow of hydrogen ions from ganymede. Geophys. Res. Lett. 24 (17), 2151–2154. http://dx.doi.org/10.1029/97GL01744.

Fray, N., Schmitt, B., 2009. Sublimation of ices of astrophysical interest: A bibliographic review. Planet. Space Sci. 57, 2053–2080. http://dx.doi.org/10.1016/j.pss.2009.09.011.

Galli, A., Vorburger, A., Wurz, P., Cerubini, R., Tulej, M., 2018. First experimental data of sulphur ions sputtering water ice. Icarus 312, 1–6, arXiv:1804.09435.

Galli, A., Vorburger, A., Wurz, P., Galand, M., Oza, A., Fatemi, S., Plainaki, C., Mura, A., 2021. Interactions between the space environment and Ganymede's surface. In: Ganymede. Cambridge University Press, (submitted for publication).

Galli, A., Vorburger, A., Wurz, P., Tulej, M., 2017. Sputtering of water ice films: A re-assessment with singly and doubly charged oxygen and argon ions, molecular oxygen, and electrons. Icarus 291, 36–45. http://dx.doi.org/10.1016/j.icarus.2017.03.018.

Grasset, O., Dougherty, M.K., Coustenis, A., Bunce, E.J., Erd, C., Titov, D., Blanc, M., Coates, A., Drossart, P., Fletcher, L.N., Hussmann, H., Jaumann, R., Krupp, N., Lebreton, J.-P., Prieto-Ballesteros, O., Tortora, P., Tosi, F., Hoolst, T.V., 2013. Jupiter ICy moons explorer (JUICE): An ESA mission to orbit ganymede and to characterise the Jupiter system. Planet. Space Sci. 78, 1–21. http://dx.doi.org/10.1016/j.pss.2012.12.002.

Gurnett, D.A., Kurth, W.S., Roux, A., Bolton, S.J., Kennel, C.F., 1996. Evidence for a magnetosphere at ganymede from plasma-wave observations by the galileo spacecraft. Nature 384, 535–537.

Hall, D.T., Feldman, P.D., McGrath, M.A., Strobel, D.F., 1998. The far-ultraviolet oxygen airglow of Europa and Ganymede. Astrophys. J. 499 (1), 475–481. http://dx.doi.org/10.1086/305604.

Hansen, G.B., McCord, T.B., 2004. Amorphous and crystalline ice on the Galilean satellites: A balance between thermal and radiolytic processes. J. Geophys. Res. Planets 109 (E1), http://dx.doi.org/10.1029/2003JE002149.

Helfenstein, P., Veverka, J., Denk, T., Neukum, G., Head, J.W., Pappalardo, R., Galileo IMAGING Team, 1997. Dark-floor craters: galileo constraints on a ganymede regolith component. In: Lunar and Planetary Science Conference. In: Lunar and Planetary Science Conference.

Hibbitts, C.A., Pappalardo, R.T., Hansen, G.B., McCord, T.B., 2003. Carbon dioxide on Ganymede. J. Geophys. Res. (Planets) 108 (E5), http://dx.doi.org/10.1029/2002JE001956.

Huebner, W.F., Keady, J.J., Lyon, S.P., 1992. Solar photo rates for planetary atmospheres and atmospheric pollutants. Astrophys. Space Sci. 195 (1), 1–294. http://dx.doi.org/10.1007/BF00644558.

Itikawa, Y., Mason, N., 2005. Cross sections for electron collisions with water molecules. J. Phys. Chem. Ref. Data 34 (1), 1–22. http://dx.doi.org/10.1063/1.1799251.

Johnson, R.E., Carlson, R.W., Cassidy, T.A., Fama, M., 2013. Sputtering of ices. In: Gudipati, M.S., Castillo-Rogez, J. (Eds.), Astrophysics and Space Science Library. 356. http://dx.doi.org/10.1007/978-1-4614-3076-6_17.

Johnson, R., Leblanc, F., Yakshinskiy, B., Madey, T., 2002. Energy distributions for desorption of sodium and potassium from ice: The Na/K ratio at Europa. Icarus 156 (1), 136–142. http://dx.doi.org/10.1006/icar.2001.6763.

Johnson, R., Liu, M., 1996. Molecular dynamics studies of minicascades in electronically stimulated sputtering of condensed-gas solids. J. Chem. Phys. 104, 6041–6051.

Jun, I., Garrett, H.B., Swimm, R., Evans, R.W., Clough, G., 2005. Statistics of the variations of the high-energy electron population between 7 and 28 jovian radii as measured by the Galileo spacecraft. Icarus 178 (2), 386–394. http://dx.doi.org/10.1016/j.icarus.2005.01.022.

Keppler, E., Krupp, N., 1996. The charge state of helium in the Jovian magnetosphere: a possible method to determine it. Planet. Space Sci. 44 (2), 71–75. http://dx.doi.org/10.1016/0032-0633(95)00076-3.

Khurana, K.K., Pappalardo, R.T., Murphy, N., Denk, T., 2007. The origin of Ganymede's polar caps. Icarus 191 (1), 193–202. http://dx.doi.org/10.1016/j.icarus.2007.04.022.

Kieffer, H.H., Smythe, W., 1974. Frost spectra: Comparison with Jupiter's satellites. Icarus 21 (4), 506–512. http://dx.doi.org/10.1016/0019-1035(74)90153-5.

Kim, T.K., Ebert, R.W., Valek, P.W., Allegrini, F., McComas, D.J., Bagenal, F., Connerney, J.E.P., Livadiotis, G., Thomsen, M.F., Wilson, R.J., Bolton, S.J., 2020. Survey of ion properties in jupiter's plasma sheet: Juno JADE-I observations. J. Geophys. Res. Space Phys. 125 (4), http://dx.doi.org/10.1029/2019JA027696.

Kivelson, M.G., Bagenal, F., Kurth, W.S., Neubauer, F.M., Paranicas, C., Saur, J., 2004. Magnetospheric interactions with satellites. In: Bagenal, F., Dowling, T.E., McKinnon, W.B. (Eds.), Jupiter. the Planet, Satellites and Magnetosphere. 1. pp. 513–536.

Kivelson, M.G., Khurana, K.K., Russell, C.T., Walker, R.J., Warnecke, J., Coroniti, F.V., Polanskey, C., Southwood, D.J., Schubert, G., 1996. Discovery of ganymede's magnetic field by the galileo spacecraft. Nature 384, 537–541.

Kivelson, M.G., Khurana, K.K., Volwerk, M., 2002. The permanent and inductive magnetic moments of ganymede. Icarus 157 (2), 507–522.

Kliore, A.J., 1998. Satellite atmospheres and magnetospheres. Highlights Astron. 11A, 1065.

Küstner, M., Eckstein, W., Dose, V., Roth, J., 1998. The influence of surface roughness on the angular dependence of the sputter yield. Nucl. Instrum. Methods Phys. Res. B 145, 320–331.

Leblanc, F., Oza, A., Leclercq, L., Schmidt, C., Cassidy, T., Modolo, R., Chaufray, J., Johnson, R., 2017. On the orbital variability of Ganymede's atmosphere. Icarus 293, 185–198. http://dx.doi.org/10.1016/j.icarus.2017.04.025.

Lebofsky, L.A., 1977. Identification of water frost on callisto. Nature 269 (5631), 785–787. http://dx.doi.org/10.1038/269785a0.

Ligier, N., Paranicas, C., Carter, J., Poulet, F., Calvin, W., Nordheim, T., Snodgrass, C., Ferellec, L., 2019. Surface composition and properties of Ganymede: Updates from ground-based observations with the near-infrared imaging spectrometer SINFONI/VLT/ESO. Icarus 333, 496–515. http://dx.doi.org/10.1016/j.icarus.2019.06.013.

Liuzzo, L., Poppe, A.R., Paranicas, C., Nénon, Q., Fatemi, S., Simon, S., 2020. Variability in the energetic electron bombardment of Ganymede. J. Geophys. Res. Space Phys. 1–35. http://dx.doi.org/10.1029/2020JA028347.

Marconi, M., 2007. A kinetic model of ganymede's atmosphere. Icarus 190 (1), 155–174. http://dx.doi.org/10.1016/j.icarus.2007.02.016.

McConkey, J.W., Malone, C.P., Johnson, P.V., Winstead, C., McKoy, V., Kanik, I., 2008. Electron impact dissociation of oxygen-containing molecules a critical review. Phys. Rep. 466 (1–3), 1–103. http://dx.doi.org/10.1016/j.physrep.2008.05.001.

McCord, T.B., Carlson, R.W., Smythe, W.D., Hansen, G.B., Clark, R.N., Hibbitts, C.A., Fanale, F.P., Granahan, J.C., Segura, M., Matson, D.L., Johnson, T.V., Martin, P.D., 1997. Organics and other molecules in the surfaces of callisto and ganymede. Science 278 (5336), 271–275. http://dx.doi.org/10.1126/science.278.5336.271.

McCord, T.B., Hansen, G.B., Fanale, F.P., Carlson, R.W., Matson, D.L., Johnson, T.V., Smythe, W.D., Crowley, J.K., Martin, P.D., Ocampo, A., Hibbitts, C.A., Granahan, J.C., 1998. Salts on Europa's surface detected by Galileo's near infrared mapping spectrometer. Science 280 (5367), 1242–1245. http://dx.doi.org/10.1126/science.280.5367.1242.

McCord, T.B., Hansen, G.B., Hibbitts, C.A., 2001. Hydrated salt minerals on Ganymede's surface: Evidence of an ocean below. Science 292 (5521), 1523–1525. http://dx.doi.org/10.1126/science.1059916.

McGrath, M.A., Jia, X., Retherford, K., Feldman, P.D., Strobel, D.F., Saur, J., 2013. Aurora on Ganymede. J. Geophys. Res. (Space Physics) 118 (5), 2043–2054. http://dx.doi.org/10.1002/jgra.50122.

Molyneux, P.M., Nichols, J.D., Bannister, N.P., Bunce, E.J., Clarke, J.T., Cowley, S.W.H., Gérard, J.C., Grodent, D., Milan, S.E., Paty, C., 2018. Hubble space telescope observations of variations in Ganymede's oxygen atmosphere and Aurora. J. Geophys. Res. (Space Phys.) 123 (5), 3777–3793. http://dx.doi.org/10.1029/2018JA025243.

NASA, 2021. See the first images NASA's juno took as it sailed by Ganymede e. [Online] https://www.nasa.gov/feature/jpl/see-the-first-images-nasa-s-juno-took-as-it-sailed-by-ganymede. (Accessed 22 2021).

Orton, G.S., Spencer, J.R., Travis, L.D., Martin, T.Z., Tamppari, L.K., 1996. Galileo photopolarimeter-radiometer observations of jupiter and the Galilean satellites. Science 274 (5286), 389–391. http://dx.doi.org/10.1126/science.274.5286.389.

Pappalardo, R.T., Barr, A.C., 2004. The origin of domes on Europa: The role of thermally induced compositional diapirism. Geophys. Res. Lett. 31 (1), http://dx.doi.org/10.1029/2003GL019202.

Paranicas, C., Szalay, J.R., Mauk, B.H., Clark, G., Kollmann, P., Haggerty, D.K., Westlake, J., Allegrini, F., Ebert, R.W., Connerney, J.E.P., Bolton, S., 2021. Energy spectra near Ganymede from juno data. Geophys. Res. Lett. 48 (10), http://dx.doi.org/10.1029/2021GL093021.

Pilcher, C.B., Ridgway, S.T., McCord, T.B., 1972. Galilean satellites: Identification of water frost. Science 178 (4065), 1087–1089. http://dx.doi.org/10.1126/science.178.4065.1087.

Plainaki, C., Massetti, S., Jia, X., Mura, A., Milillo, A., Grassi, D., Sindoni, G., D'Aversa, E., Filacchione, G., 2020. Kinetic simulations of the jovian energetic ion circulation around ganymede. Astrophys. J. 900 (1), 74.

Plainaki, C., Milillo, A., Massetti, S., Mura, A., Jia, X., Orsini, S., Mangano, V., De Angelis, E., Rispoli, R., 2015. The H_2O and O_2 exospheres of ganymede: The result of a complex interaction between the jovian magnetospheric ions and the icy moon. Icarus 245, 306–319. http://dx.doi.org/10.1016/j.icarus.2014.09.018.

Pollack, J.B., Witteborn, F.C., Erickson, E.F., Strecker, D.W., Baldwin, B.J., Bunch, T.E., 1978. Near-infrared spectra of the galilean satellites: Observations and compositional implications. Icarus 36 (3), 271–303. http://dx.doi.org/10.1016/0019-1035(78)90110-0.

Poppe, A.R., Fatemi, S., Khurana, K.K., 2018. Thermal and energetic ion dynamics in Ganymede's magnetosphere. J. Geophys. Res. Space Phys. 123 (6), 4614–4637. http://dx.doi.org/10.1029/2018JA025312.

Reimann, C., Boring, J., Johnson, R., Garrett, J., Farmer, K., Brown, W., Marcantonio, K., Augustyniak, W., 1984. Ion-induced molecular ejection from D_2O ice. Surf. Sci. 147 (1), 227–240. http://dx.doi.org/10.1016/0039-6028(84)90177-8, URL https://www.sciencedirect.com/science/article/pii/0039602884901778.

Roth, L., Ivchenko, N., Gladstone, G.R., Saur, J., Grodent, D., Bonfond, B., Molyneux, P.M., Retherford, K.D., 2021. Evidence for a sublimated water atmosphere on ganymede from hubble space telescope observations. arXiv e-prints. arXiv:2106.03570.

Shematovich, V.I., 2016. Neutral atmosphere near the icy surface of Jupiter's moon Ganymede. Solar Syst. Res. 50 (4), 262–280. http://dx.doi.org/10.1134/S0038094616040067.

Shi, M., Baragiola, R.A., Grosjean, D.E., Johnson, R.E., Jurac, S., Schou, J., 1995. Sputtering of water ice surfaces and the production of extended neutral atmospheres. J. Geophys. Res. 100 (E12).

Shi, J., Teolis, B.D., Baragiola, R.A., 2009. Irradiation-enhanced adsorption and trapping of O_2 on nanoporous water ice. Phys. Rev. B 79 (235422), http://dx.doi.org/10.1103/PhysRevB.79.235422.

Shoemaker, E.M., Lucchitta, B.K., Wilhelms, D.E., Plescia, J.B., Squyres, S.W., 1982. The geology of Ganymede. In: Satellites of Jupiter. pp. 435–520.

Sigmund, P., 1981. Sputtering by ion bombardment theoretical concepts. In: Behrisch, R. (Ed.), Sputtering By Particle Bombardment I: Physical Sputtering of Single-Element Solids. Springer Berlin Heidelberg, Berlin, Heidelberg, pp. 9–71. http://dx.doi.org/10.1007/3540105212_7.

Smith, B.A., Soderblom, L.A., Beebe, R., Boyce, J., Briggs, G., Carr, M., Collins, S.A., Cook, I., Danielson, G.E., Davies, M.E., Hunt, G.E., Ingersoll, A., Johnson, T.V., Masursky, H., McCauley, J., Morrison, D., Owen, T., Sagan, C., Shoemaker, E.M., Strom, R., Suomi, V.E., Veverka, J., 1979. The Galilean satellites and Jupiter: Voyager 2 imaging science results. Science 206 (4421), 927–950. http://dx.doi.org/10.1126/science.206.4421.927.

Spencer, J.R., 1987. Icy Galilean satellite reflectance spectra: Less ice on Ganymede and Callisto? Icarus 70 (1), 99–110. http://dx.doi.org/10.1016/0019-1035(87)90077-7.

Stephan, K., Hoffmann, H., Hibbitts, C.A., Wagner, R., Jaumann, R., 2017. Ice particle size variations and possible non-ice materials on ganymede's and callisto's surface. In: AAS/Division for Planetary Sciences Meeting Abstracts #49. In: AAS/Division for Planetary Sciences Meeting Abstracts, vol. 49.

Teolis, B.D., Plainaki, C., Cassidy, T.A., Raut, U., 2017. Water ice radiolytic O_2, H_2, and H_2O_2 yields for any projectile species, energy, or temperature: A model for icy astrophysical bodies. J. Geophys. Res. Planets 122 (10), 1996–2012. http://dx.doi.org/10.1002/2017JE005285.

Turc, L., Leclercq, L., Leblanc, F., Modolo, R., Chaufray, J.-Y., 2014. Modelling ganymede's neutral environment: A 3D test-particle simulation. Icarus 229, 157–169. http://dx.doi.org/10.1016/j.icarus.2013.11.005.

Vorburger, A., Pfleger, M., Lindkvist, J., Holmström, M., Lammer, H., Lichtenegger, H.I.M., Galli, A., Rubin, M., Wurz, P., 2019. Three-dimensional modeling of Callisto's surface sputtered exosphere environment. J. Geophys. Res. (Space Phys.) 124 (8), 7157–7169. http://dx.doi.org/10.1029/2019JA026610.

Vorburger, A., Wurz, P., 2018. Europa's ice-related atmosphere: The sputter contribution. Icarus 311, 135–145. http://dx.doi.org/10.1016/j.icarus.2018.03.022.

Vorburger, A., Wurz, P., Lammer, H., Barabash, S., Mousis, O., 2015. Monte-Carlo Simulation of Callisto's exosphere. Icarus 262, 14–29. http://dx.doi.org/10.1016/j.icarus.2015.07.035.

Wurz, P., Rohner, U., Whitby, J.A., Kolb, C., Lammer, H., Dobnikar, P., Martín-Fernández, J.A., 2007. The lunar exosphere: The sputtering contribution. Icarus 191, 486–496. http://dx.doi.org/10.1016/j.icarus.2007.04.034.

Yung, Y., McElroy, M., 1977. Stability of an oxygen atmosphere on ganymede. Icarus 30 (1), 97–103. http://dx.doi.org/10.1016/0019-1035(77)90124-5.